Mechanical compaction mechanisms in the input sediments of the Sumatra Subduction Complex- insights from microstructural analysis of cores from IODP Expedition- 362

Sivaji Lahiri[1]*, Kitty L. Milliken[2], Peter Vrolijk[3], Guillaume Desbois[1], Janos L. Urai[1]

[1]Institute of Tectonics and Geodynamics, RWTH Aachen University, Germany, Lochnerstrasse 4–20, 52056, Aachen, Germany

[2]Bureau of Economic Geology, The University of Texas at Austin, Austin, TX, 10611, USA

[3]Applied Ocean Science and Engineering, Woods Hole Oceanographic Institution, Woods Hole, MA, United States

* Corresponding author: sivaji.lahiri2@gmail.com

Abstract

The input sediments of the North Sumatra subduction zone margin, drilled during IODP Expedition 362, exhibit remarkable uniformity in composition and grain size over the entire thickness of the rapidly deposited Nicobar Fan succession (sea-floor to 1500 mbsf depth), providing a unique opportunity to study the micromechanisms of compaction. Samples were prepared from dried core samples from sites (U1480 and U1481) by both Ar-ion cross-section polishing and broad-ion beam cutting, and imaged with a field-emission SEM. Shallowest samples (sea-floor to 28mbsf) display a sharp reduction in porosity from 80% to 52% due to collapse of large clay-domain/matrix pores associated with rotation and realignment of clay-platelets parallel to the bedding plane. The deeper succession (28mbsf to 1500mbsf) exhibits less rapid reduction in porosity from 52% to 30% by the progressive collapse of silt-adjacent larger pores by bending and subsequent sliding/fracturing of clay particles. In addition, there is a correlated loss of porosity in the pores too small to be resolved by SEM.

Clastic particles show no evidence of deformation or fracturing with increasing compaction. In the phyllosilicates, there is no evidence for pressure solution or recrystallization: thus, compaction proceeds by micromechanical processes. Increase in effective stress up to 18 MPa (~1500mbsf) causes the development of a weakly aligned phyllosilicate fabric defined by illite clay particles and mica grains, while the roundness of interparticle pores decreases as the pores become more elongated. We propose that bending of the phyllosilicates by intracrystalline slip may be the rate-controlling mechanism.

Pore size distributions show that all pores within the compactional force chain deform, irrespective of size, with increasing compactional strain. This arises because the force chain driving pore collapse is localized primarily

within the volumetrically dominant and weaker clay-rich domains; pores associated with packing around isolated silt particles enter into the force chain asynchronously and do not contribute preferentially to pore loss over the depth range studied.

Introduction

Muds are fine-grained sediments (>50% of particles <63μm diameter) comprising platy detrital clay minerals and equidimensional detrital grains such as quartz, feldspar, calcite, etc. (Nakano, 1967; Hesse, R., 1975; Sintubin, 1994). Understanding the mechanical, chemical, and microstructural properties of mud and mudstone is of great interest for rock property prediction in basic earth science, in exploration, subsurface integrity studies and geotechnical engineering (Yagiz, S., 2001; Aplin and Yagiz, 2011; Lazar et al., 2015). The chemical and physical behavior of marine muds plays a critical role in defining the geometry of accretionary prisms, locating the décollement for fault rupture (Vrolijk, 1990; Chester et al., 2013) and understanding subduction zone earthquakes and tsunamis (Dean et al., 2010; Chester et al., 2013; Hüpers et al., 2017).

Marine mud is deposited with a highly porous isotropic fabric (Bowles, 1969; Bennett et al. 1981; Bennett et al. 1991); depositional porosity in mud is about twice as high as in sand (e.g., Velde, 1996, Lundegard, 1992). In contrast, mudstones have low porosities, modal pore sizes measured in nm, and an absence of textural controls on porosity (e.g. Aplin et al., 2006; Milliken et al., 2012; Milliken et al., 2013). The processes in this dramatic evolution of porosity has similarities to compaction of sand to sandstone, comprising a combination of compaction and cementation (Milliken and Day-Stirrat, 2013), although the much smaller, elongated phyllosilicate grains increase the role of clay-bound water in the process (Karaborni et al., 1996). Whereas a refined and somewhat predictive understanding exists for porosity evolution in sand and sandstones (e.g., Lander and Walderhaug, 1999; Paxton et al., 2002; Lander et al., 2008; Adjukiewicz and Lander, 2010, Desbois et al., 2011), such a model is at best preliminary for muds and mudstones (Pommer and Milliken, 2015; Milliken and Olson, 2017). It seems clear that the composition of the grain assemblage importantly sets the stage for porosity evolution in muds (Milliken, 2014), cementation being the greatest in muds with abundant biogenic debris. In contrast to sandstones, however, cementation is far less common globally in mudstones (Milliken, 2019), leading to the notion that mechanical compaction may be far more important in muds. Establishing the expected compaction behavior for muds in a setting of well-constrained mud properties is an essential contribution that our study hopes to serve.

Investigations of mud and mudstone compaction are usually based on proxy data, such as velocity or density, rather than direct measurements of porosity (e.g., references in Mondol, 2007). Direct measurement of porosity can be broadly classified into two categories: 1) laboratory experiments; (e.g., Mitchell, 1956; Bennett et al. 1981; Vasseur et al. 1995; Mondol et al. 2007; Fawad et al. 2010; Emmanel and Day-Stirrat, 2012), and 2) studies on natural samples (e.g., Meade, 1964; Ho et al., 1999; Aplin et al. 2003, 2006; Day-Stirrat et al., 2008; 2010; 2012; Milliken et al, 2012, Milliken et al., 2013). A common shortcoming of studies on natural samples is the assumption that the bulk porosity is a direct measure of compaction although porosity loss has contributions of both compaction and cementation (Lundegard, 1992; Ehrenberg, 1989; Paxton et al., 2002), and this can only be accomplished by petrographic inspection (Milliken and Curtis, 2017). Experimental studies generally avoid this shortcoming by the use of lab-produced particle packs that undergo no chemical change during the experiment.

Studies of shallowly buried units (like the present study) are the ones most likely to avoid the complication of cementation, especially if temperatures are low and bulk grain assemblages are siliciclastic (Milliken, 2014).

Previous studies report contrasting ideas about the mechanisms of mechanical compaction of mud. According to some studies, burial compaction significantly increases the alignment of phyllosilicate (clay and mica) parallel to the bedding planes (Bowles et al., 1969; Oertel and Curtis, 1972; Vasseur et al., 1995). Other studies state that intense mechanical compaction has a limited impact on the development of phyllosilicate fabric in mud (Ho et al., 1999; Aplin et al., 2006; Day-Stirrat et al., 2008; 2011). These studies investigated the changes in particle alignment and reduction in porosity (Ho et al., 1999; Aplin et al., 2006; Day-Stirrat et al., 2008; 2011) but without imaging the evolution of pore morphology with increasing compactional strain. This is where this study aims contribute.

We received 55 mud samples from drill cores collected during IODP Expedition 362 west of the North Sumatra subduction zone margin and investigated the evolution of petrographic microstructure and pore morphology as a function of compactional strain. Apart from general implications for global mudrocks, we hope this investigation will also contribute to studies that seek to predict rock properties in the deeper subsurface at the Sumatra subduction front.

Geological background and drilling

The Sumatra subduction zone extends 5000km from the Andaman-Nicobar Islands in the northwest to the Java-Banda arc in the Southeast (Fig.1a and b) (Prawirodirdjo et al., 1997; Hippchen and Hyndman, 2008). The trench of the Sumatra subduction zone (Fig.1a) developed on the subducting Indo-Australian Plate at a convergence rate of 5.5 cm/yr in the north and 7.23 cm/yr in the South (Ghosal et al., 2014; Moeremans, and Singh, 2015).

On 26th December 2004, the west coast of Northern Sumatra recorded one of the largest earthquakes (Mw-9.3) in the 21st century, generating a devastating Tsunami in the Indian Ocean (Ammon et al., 2005; Lay et al., 2005). Understanding the mechanism(s) behind this unprecedented event was the central idea behind IODP Expedition 362. The main objective of the expedition was to collect core and log data of the incoming sedimentary succession of the Indo-Australian oceanic plate to understand the seismogenic process related to the margin (Dugan et al., 2017; McNeill et al., 2017). During the expedition in 2016, drilling was performed on two sites (U1480 and U1481) located on the oceanic plate west of the North Sumatra subduction margin and east of the Ninety East Ridge (Fig.1a, b) (Dugan et al., 2017). The drilling sites recovered a complete, 1.5 km thick sedimentary section from late Cretaceous to Pleistocene down to the basement of basaltic crust (Dugan et al., 2017; McNeill et al., 2017).

The input sedimentary section of the Sumatra subduction zone comprises the distal part of the trench wedge, Nicobar fan sequence, and pre-fan pelagic section on the basaltic crust at the bottom (Dugan et al., 2017; McNeill et al., 2017). At Site U1480, the entire recovered section was categorized into six lithological entities, Units I to VI (Fig. 1c) (McNeill et al., 2017). Unit I (0 to 26.72 mbsf) consists of unconsolidated calcareous clay, silty clay with alternating fine sand (McNeill et al., 2017). Unit II from 26.72 to 1250 mbsf consists of alternating fine-grained sand and silty clay to silt (McNeill et al., 2017). Unit III (1250 ~ 1327 mbsf) is divided into two subunits: Unit IIIA and IIIB (McNeill et al., 2017). Unit IIIA consist of thin to medium-bedded, gray-green or brown mudstone and intercalated siltstone, and Unit IIIB is composed of reddish-brown tuffaceous silty claystone with fragmented sponge spicules and radiolaria (McNeill et al., 2017). The boundary between Units IIIA and IIIB (1310 mbsf) at this site marks the base of the Nicobar Fan and the beginning of the thin pre-fan succession (Pickering et al., 2020). Units IV, V, and VI include volcanoclastic rocks with tuffaceous sandstone, conglomerates, and basaltic oceanic crust, respectively. For this study, we restricted ourselves to the Nicobar fan sequence that comprises Unit I, II, and IIIA. At Site U1481, the pre-fan succession was not encountered and a Unit III, a thicker equivalent of Subunit IIIA at Site U1480, represents the material of the lower Nicobar Fan (see Figure F15, in Site U1481 report; McNeil et al., 2017).

X-ray diffraction (XRD) and bulk rock analysis at Site U1480 (in Units I and II) show a clay mineral assemblage dominated by illite, with minor smectite and chlorite (Supplementary data-1) (Rosenberger et al., 2020). The smectite content decreases with depth with the mean value of 33 wt% in Unit I and 17 wt% in Unit II (Table 1) (Rosenberger et al., 2020). However, the relative abundance of smectite content increases sharply in Unit IIIA with a mean value of 73 wt%. The illite percentage in the clay assemblage increases down section from Unit I to Unit II from a mean of 49 wt% to 59 wt%; whereas decreases in Unit IIIA with a mean of 19 wt%. The expandability of the illite/smectite mixed-layer increases down-section, which signifies an opposite trend to the one expected for burial diagenesis (Rosenberger et al., 2020). Clay mineralogy in the lower fan muds of Unit III of Site U1481A contains an average of 37 percent smectite and 37 percent illite (Rosenberger et al., 2020).

The Nicobar fan sequence exhibits almost compositionally homogeneous (silt/clay ratio; mostly 'silty-clay') subunits with uniform grain size (McNeill et al., 2017), and also a history of rapid deposition (125-290 m/my; Backman et al., 2019). The drilling sites are 255 km away from the deformation front, thus the samples are undisturbed by tectonic faulting. In addition, the scarcity of biogenic grains and low temperatures (<68°C) make cementation only as highly localized concretions (McNeil et al., 2017; Torres and Milliken, 2019). Such a homogeneous sedimentary secession extending across 1.5 km depth is rare in sedimentary basins. Hence, these samples provide us with a unique opportunity to study depth-wise variation in microstructure as a function of vertical effective stress with few complications from multiple causes of porosity loss.

Sampling and Methods

This study is based on two sample sets that were obtained from Sites 1480 (Holes E, F, G, and H) and 1481 (Hole A) independently, and analyzed by slightly different methods. The first sample set (33 mud samples; depth 1.24 to 1300 mbsf) was prepared and analyzed using BIB-SEM at RWTH Aachen University, Germany. The second sample set (22 samples; depths 6.25 to 1493.30 mbsf) was prepared using Ar-ion cross-section polishing and imaged by field-emission SEM at the Bureau of Economic Geology (BEG) at the University of Texas at Austin. Core description of the analysed 55 mud samples are tabulated in Supplementary data-2.

BIB-SEM technique (analysis of the first set of samples, Aachen University)

Sample preparation for BIB-SEM and imaging

We received 33 freeze-dried mud samples from the IODP repository, Japan (SN-1 to SN-33 in Table-1). The samples were collected using a tube inserted perpendicular to the cut face of the drill core in such a way that the notch of the tube identified the top of the sample so the orientation of bedding planes for each sample was known. In Fig. 1d, a tube sample received from the IODP repository is shown, where the red line on the top of the tube identifies the notch. Subsamples (10 x 5 x 2 mm^3) were cut from the individual freeze-dried samples using a razor blade. These subsamples were pre-polished using silicon carbide (SiC) paper to reduce the roughness of the surface down to 10 μm. Further, Broad Ion Beam (BIB) polishing was carried out using a JEOL SM-09010 cross-section polisher for 10 hours at 6 kV and 150 μA. BIB reduces surface damage by removing a 100 μm thick layer to generate a high-quality polished cross-section of 1-2 mm^2 with a topography less than 5 nm (Desbois et al., 2009).

After polishing, the BIB cross-sections were coated with tungsten and imaged with a Zeiss Supra 55 SEM with SE2, BSE, and EDX detector (Supplementary data-3). SE2 images were used to image porosity, while for identifying phases BSE images are combined with an EDX map as well as EDX point analysis. For each cross-section, we made mosaics of hundreds of SE2 and BSE images at a magnification of 20,000x (~14.3 nm pixel value) and 10,000x respectively, with an overlap of 20% to 30%, (Klaver et al., 2012; 2015; 2016; Hemes et al., 2013; 2015; 2016; Laurich et al., 2014). The mosaics are stitched together using Aztec software preserving the original pixel resolution. Finally, these stitched images are used for the segmentation of pore spaces, minerals, and other respective analyses.

Image segmentation and pore analysis

For quantifying porosity and pore morphology, individual SE2 image mosaics were segmented using a 'seed and grow' algorithm (Adams and Bischof (1994)) implemented with a MatLab code (Jiang et al., 2015; Schmatz et al., 2016) (Supplementary data-3). The 'seed and grow' algorithm works based on the difference in intensity of greyscale value in an image (Bright = minerals, dark= pores). After automatic segmentation, individual pores in SE2 images are manually corrected if required.

Similarly, using ImageJ software (threshold toolbox and machine learning algorithm), segmentation of the individual mineral phases was carried out combining BSE images and EDX elemental maps. While quartz, calcite, pyrite, mica minerals are efficiently segmented using these tools, feldspars are found difficult to segment because of similar composition as clay (Supplementary data-4, 5 and 6). Finally, corrected pore segmented SE2 mosaics are overlaid on the phase maps using the 'georeference' tool of QGIS (http://qgis.osgeo.org), (Supplementary data-4, 5 and 6).

Pore detection resolution (PPR) and representative area analysis (REA)

'Practical pore detection resolution' (PPR) indicates the pore sizes above which one can assume to detect 100% of the pores present in the SE2 mosaic (Klaver et al., 2012). In agreement with earlier results using this instrument (Klaver et al., 2012; 2015; 2016; Hemes et al., 2013; 2015; 2016; Laurich et al., 2014), we found PPR of ~2000

Need to provide assumptions, errors and limitations of determining porosity + pore sizes from 2D images.

nm^2 and ~8500 nm^2 for the magnification of 20,000x and 10,000x images, respectively, corresponding to 10pixel size in an image.

After segmenting all minerals, representative elementary area analysis (REA) was performed using the box counting technique on mineralogical phase maps (Kameda et al., 2006; Klaver et al., 2012). Similar steps are also followed for determining a representative elementary area for SE2 images. The estimated REA values using SE2 and BSE mosaics for the analysed 33 mudstone samples are documented in Supplementary data-7.

Ion polishing and SEM technique (second set of samples; BEG, UT Austin).

22 Samples (SN-34 to SN-55 in Table-1) were taken shipboard from the sample half of the still-wet core in small plastic tubes (similar to the ones used for the sample set at Aachen) inserted into the core by manual pressure. The tubes were removed from the core and sealed in plastic bags. In the laboratory at the BEG, sample bags were opened and the muds were allowed to dry slowly in the tubes over several weeks. No discernible shrinkage was observed as the dried core pieces still fully filled the tubes. The tubes were carefully removed and a small cube (approximately 0.5 to 1 cm^3) was cut using a sharp knife and small hand saws; an orientation mark was placed on the cube to indicate the bedding direction. Bed-perpendicular surfaces were prepared by Ar-ion cross-section polishing, using the Leica EM TIC020 triple ion beam miller and coated with Ir for imaging. Manual placement of the cut cubes into the ion mill is not precise so the ion-polished surfaces have slight variation from perpendicular to bedding. Pore imaging was performed on the FEI Nova NanoSEM 430 using the in-lens SE detector, a 30 μm aperture, 15 KeV accelerating current, a working distance of around 5–6 mm, and an intermediate-range sample current (spot size = 3, mid-range for the instrument). Randomly selected views (typically 3-6) of all samples were collected at 6kx machine magnification; additional views illustrating pore types and pore/grain relationships were made at 10kx to 30kx (machine magnification).

Results

should be briefly described as to methodology in the above section with a refer to the paper with full details.

Estimating compaction strain from MAD-porosity data

Shipboard MAD (moisture and density) porosity versus depth data for mud samples exhibits a sharp reduction in porosity from 80% to 52% from the seafloor to 28 mbsf (Fig.2a). Deeper samples display a comparatively smaller reduction in porosity of approximately from 52% to 30% over a depth range of 28 to 1500 mbsf (Fig.2a and b).

We calculated compaction strain using the shipboard MAD porosity data following a method proposed by Nollet et al., 2005, and subsequently used by Neagu et al., 2010 (Fig.2c and d), assuming 1D consolidation and no change in solid volume. The compaction strain (ε_c) is then computed as:

not in refs

$$\varepsilon_c = \frac{1-\phi_0}{1-\phi_1} \qquad \text{(Eqn-1)}$$

Here ϕ_0 = initial porosity, and ϕ_1 = final porosity. Our samples from sites U1480 and U1481 show no evidence of tectonic faults (McNeill et al., 2017), supporting our assumptions. We considered the initial porosity ϕ_0 as the MAD porosity at 0.6 mbsf depth ($\phi_0 = 80\%$). Compaction strain following Eqn-1 (Supplementary data-7), is

Figure 2 shows some cemented samples (concretions) so should be mentioned in the text. Also, the yellow symbols on Figure 2 are not explained at all, other than as being measured for something at Aachen BES.

plotted against depth in Fig. 2c and d. Compaction strain increases from 1 to 2.05 from the seafloor to 28 mbsf (i.e. Unit I), and from 2.00 to 3.05 from 28mbsf to 1500 mbsf (Fig. 2c and d).

Another common measure of compaction is the intergranular volume (IGV; Paxton et al 2002), which corresponds to the sum of intergranular porosity and intergranular cement. In some mudstones, it may be necessary to calculate IGV differently because of the presence of abundant primary intragranular pores and pore-filling bitumen (Milliken and Olson, 2017). In our sample set, cement is absent, and IGV is taken to equal the bulk porosity from shipboard MAD measurements.

Compactional porosity loss (COPL), referenced against the original sediment volume, is calculated from the initial primary intergranular porosity (Pi; 80% in this case) and the IGV as follows (Lundegard, 1992; Ehrenberg, 1989):

$$COPL= Pi-(((100-Pi) \times IGV)/(100-IGV)) \quad \text{(Eqn-2)}$$

At an IGV of 50%, COPL is 60%; in the deepest samples in the Nicobar fan (IGV of around 30%) COPL is 70% (supplementary data-7). Contribution of cementation (CEPL) is absent in the absence of observed cements.

Description of grain microstructure and pore morphology

To have consistency in the data set, we prepared SE2 mosaics for all samples from the Aachen sample set at 20,000x magnification covering an average 100×100 μm^2 area (Supplementary data-7). In addition, to examine the effect of magnification on BIB-SEM porosity and representative area analysis (REA), three samples (i.e. SN-7, SN-15, and SN-29) were also imaged each at 5,000x and 10,000x magnification (Supplementary data-7), respectively. A decrease in magnification and resolution reduces visible BIB-SEM porosity.

We observed consistent results for the REA analysis. For SE2 mosaics, REA varies between 45×45μm^2 to 85×85 μm^2 at 20,000x magnification, and for segmented phase maps, REA varies between 90×90 μm^2 to 130×130 μm^2 at 10,000x magnification (Supplementary data-7). In the UT sample set, the standard images taken at 6kx with machine magnification are 49.7x45.7 μm^2, so these images are also within the estimated REA range.

Six mineral phases occur in significant amounts in the Sumatra samples, as detrital particles: quartz, feldspar (K-feldspar, albite, and Ca-plagioclase), calcite, micas (muscovite, biotite, and chlorite), and detrital clay clay-size particles, which are dominantly illite. The average clay percentage in these mudstone samples varies between 65% to 75%. Samples SN-1 (77%) and SN-4 (76%) are slightly enriched in clay content, whereas SN-7, SN-9, SN-17, SN-28, SN-29, and SN-31 contain less clay (<65%) (Supplementary data-7).

Using BIB-SEM and automatic pore segmentation techniques, an average of >30,000 pores have been detected for each individual sample in the Aachen sample set at 20,000x magnification. Correlating with the MAD data set, the estimated BIB-SEM porosity reduces from 32% to 19% over a depth range of seafloor to 28 mbsf, while the deeper samples display a smaller reduction from 19% to 10% over a depth range of 28 to 1500 mbsf respectively (Fig.3a). Consistent with numerous previous studies, the results document a mismatch between bulk measured porosity (MAD) and imaging porosity (BIB-SEM) (e.g., Hemes et al., 2013; Houben et al., 2014; Nole et al., 2016;

not in refs

Olkar et al., 2019) (Supplementary data-7). We plotted BIB-SEM porosity vs MAD porosity and found an approximately linear correlation (Fig. 3b).

Type of pores

Intergranular pores contribute >99% of the total visible porosity (Fig.4). Intragranular pores (see below) are rare. The size and shape of inter-granular pores change during compaction (Table 2).

Intergranular pores are classified based on grain size (irrespective of mineralogy): 1) Clay domain (matrix) pores, and 2) Silt-adjacent pores. Based on the variation in size, clay domain pores divided further into: 1) Large clay domain pores; pore size >5x10^5 nm^2, and the pore boundary is defined by more than three clay particles, and 2) small clay domain pores; the pore size <5x10^5 nm^2 and generally occur in between two/three clay particles (see further detail below). Large and small clay domain pores are classified by geometry as: 1) Elongate pores (aspect ratio >3:1) and, 2) equant-shaped pores (aspect ratio <3:1). Elongate pores consist of: 1) linear-elongated pores, and 2) crescent-shaped elongated pores. Examples of different clay-domain pore types are shown in Fig. 5, 6, and 7.

Silt-adjacent are categorized as two types: 1) large silt-adjacent pores are >5x10^5 nm^2, and pore boundaries are defined by more than three particles; and 2) small silt-adjacent pores include pore sizes <5x10^5 nm^2, and pore boundaries are defined by two/three particles (see further detail on the modal sizes of these pore types below). Large and small silt-adjacent pores are either: 1) Equant shaped (aspect ratio <3:1) or 2) elongated (aspect ratio >3:1). Further, elongated silt-adjacent pores consist of: 1) linear-shaped elongated pores and 2) crescent-shaped elongated pores. These pore types are highlighted in Fig. 5, 6, and 7.

Change in inter-particle pore morphology with depth

Seafloor to 28mbsf (Unit I)

The shallow mud samples in Unit I are unconsolidated and highly porous (Fig. 5a; Supplementary data 8). Sample SN-1 (1.24 mbsf) has a maximum MAD porosity of 80%. We observe three types of clay particle contacts in the microstructure of SN-1; edge to edge (EE), edge to face (EF), and face to face (FF) contacts. Among them, EF and FF contacts are abundant and EE contacts are rare (Table 1). The sample exhibits abundant large clay domain pores and large silt-adjacent pores that are equant with smooth edges and a rounded pore perimeter. The sample also contains abundant linear-elongated and equant-shaped small clay-domain pores. Crescent-shaped small clay domain pores are rare in the microstructure of this sample. Equant-shaped, small silt-adjacent pores are abundant. In addition, linear elongated and crescent-shaped small, silt-adjacent pores are also commonly observed (Fig.5a; Table 2).

With increasing compaction strain (ε_c = 1.119) and depth (5.1 mbsf; Supplementary data 8), porosity (MAD) reduces to 75% and corresponding COPL=19% (sample SN-2; Fig. 5b). The microstructure of SN-2 displays almost similar characteristics as observed in the earlier sample SN-1, although there are fewer large clay domain pores in SN-2 than SN-1. Linear elongated and equant-shaped small clay domain pores are common (Table 2), but crescent-shaped small clay domain pores are rare. The microstructure of SN-2 exhibits abundant equant-shaped large and small silt-adjacent pores.

With an increase in compaction strain to ε_c ~2.00 (28 mbsf), the sample microstructure is dominated by FF contacts (Fig. 5c). and EE and EF contacts are rare (Table 3). Additionally, large clay-domain pores become sparse or infrequent in the microstructure (Fig. 8). Crescent-shaped, small clay domain pores in the microstructure are rare, whereas equant-shaped small clay domain pores are common. Both small and large silt-adjacent pores exhibit equant shapes (Fig. 8d, e and f). The sample analysed at the base of Unit I (SN-6; 28 mbsf) contains rare large clay-domain pores and abundant FF contacts (Fig. 5c; MAD porosity = 54% and COPL = 55%).

28 mbsf to 1500 mbsf (Units II and III)

Mud samples from the lower part of the Nicobar fan section are more compacted than shallower samples. We analyzed a total of 29 samples using BIB-SEM at Aachen and 18 samples using the field emission SEM at UT Austin from this section. An increase in compactional strain from 2.00 to 3.15 over a depth range of 28 to 1500 mbsf causes a porosity reduction (MAD) of 54% to 28%, and the corresponding change in average COPL is 55% to 72%. The microstructure of these samples is dominated by FF contacts among clay particles; EF and EE contacts are rare (Table 3; Fig. 6 and 7 b, c). All samples exhibit abundant small linear-elongated clay domain pores between two parallel clay sheets (Fig. 8b). Equant-shaped small, clay domain pores are rarely observed below 150 mbsf depth (ε_c>2.4). Crescent-shaped, small, clay domain pores are rare at shallow depth but become abundant with an increase in compactional strain ε_c >2.95 (871.87 mbsf) as the surrounding clay particles are bent (Fig.6; Supplementary data 9). In addition, large clay domain pores in these samples are rarely observed in the vicinity of silt clasts (Table 2).

Below 100 mbsf (ε_c =2.20), silt-adjacent small pores are dominantly equant shaped, but below 300 mbsf (ε_c >2.5) silt-adjacent small pores are dominantly linear-elongated (Fig. 8e). Crescent-shaped, small, silt-adjacent pores are common in all samples. Large silt-adjacent pores are dominantly equant above 200 mbsf depth (ε_c <2.40) and commonly linear-elongate below 400 mbsf depth (ε_c >2.5) (Fig.8f). It appears that due to an increase in compactional strain the shape of the silt-adjacent pores changes from equant to linear-elongated (Table 2). In samples with more silt, equant-shaped small and large, silt-adjacent pores can persist at greater depths (Fig. 8e and f).

Below 28 mbsf (ε_c >2.0), the number of large silt-adjacent pores in the microstructure decreases. Comparing samples SN-8 (74.07 mbsf and ε_c =2.09) and SN-32 (1267.14mbsf and ε_c =3.15) illustrates how the number of large, silt-adjacent pores decreases with depth (Fig. 6a, and c) when the clay fraction (Supplementary Data 7) is comparable. This relationship is apparent even in samples separated by a smaller depth difference (SN-49 from 959.14 mbsf and SN-55 from 1433.36 mbsf; Fig. 7b and c). While the number of large pores diminishes, the maximum size of the large silt-adjacent pores remains constant (10^7 nm^2; Supplementary data 10).

Intra-particle and intra-crystalline pores

Intraparticle pores are observed in microfossils, authigenic pyrite framboids, equant-shaped dolomite, calcite, quartz, mica, and lithic grains. Two different types of intraparticle pores were found in microfossils; elongated pores (Supplementary data 11a and c) and large rounded pores (Supplementary data 11b and d). The typical size of the elongated and Rounded pores in microfossils (10^5 nm^2) are larger than elongated pores (10^3 nm^2). While intraparticle pores in microfossils and most detrital grains are present at deposition, intraparticle pores in many mica grains form during burial and are considered secondary pores. Intraparticle pores in micas have cleavage-parallel, elongated pores with an aspect ratio >7 (Supplementary data 11e), and are interpreted to open by bending of the micas during compaction (Supplementary data 11f).

Variation in the orientation of pores and grains due to compactional strain

We examined the change in orientation of the long axis of pores with increasing compaction strain. For all segmented pores, the angle between the long axis and the bedding plane was determined and plotted in rose diagrams (Supplementary data-12). Samples from the seafloor to 28 mbsf exhibit a weak preferred orientation of the long axis of pores with maxima oriented obliquely to the bedding planes. However, below 28 mbsf the samples have a preferred orientation of the long axis of pores aligned subparallel to the bedding plane Further, due to an increase in vertical effective stress down section below 28 mbsf in Units II and III, the degree of preferred alignment of the long axis of pores only increases a small amount (Supplementary data-12).

We determined the angle between the long axis of individual silt grains and the bedding plane for all samples and plotted the angle in a rose diagram (Supplementary data-12). For quartz, feldspar, and calcite the degree of preferred orientation of the long axis of grains changes little with depth. However, the rose diagrams obtained for mica show a weak maxima parallel to the bedding plane and several submaxima oriented obliquely to the bedding plane above 28 mbsf. Preferred alignment of the long axis of mica grains increases at 28 mbsf with a strong maximum oriented parallel to bedding plane. Below 28 mbsf, further increase in the degree of preferred alignment is small.

Size distribution of pores

Pore size distributions (Fig.9) of shallow samples (Unit I) are trimodal. Sample SN-1 has peaks between 10^5 to 10^6 nm^2, 10^6 to 10^7 nm^2, and 10^7 to 10^8 nm^2, and SN-2 has peaks from 10^4 to 10^5 nm^2, 10^5 to 10^6 nm^2, and 10^6 to 10^7 nm^2. These three pore size regimes correspond to the small clay domain and silt-adjacent pores, large clay domain pores, and large silt-adjacent pores. Samples from Units II and III exhibit bimodal pore size distributions (SN-10, SN-26, and SN-33 in Fig.9). SN-10 has a peak between 10^5 to 10^6 nm^2, corresponding to small clay domain and silt-adjacent pores, and 10^6 to 10^7 nm^2, reflecting large silt-adjacent pores. Large clay domain pores are absent from samples below 28mbsf depth (Units II and III) based on the pore size distributions combined with image analysis. At the shallow depth, contribution to total porosity by larger silt adjacent pore is greater compared to the contribution by small clay domain pores (Fig.9 e and g). The contribution of large, silt-adjacent pores to total porosity diminishes with depth. Hence, at greater depth, contribution to total porosity by larger silt adjacent pore is less compared to small clay domain pores (Fig.9i).

Pore size distributions follow a power-law shown on a double logarithmic graph following the equations (Klaver et al., 2012; 2015; 2016; Hemes et al., 2013; 2015; 2016; Laurich et al., 2014):

$$\frac{N_i}{b_i S_{mosaic}} = CS_{Pore}{}^{D} \quad \text{(Eqn-3)}$$

$$\log\left(\frac{N_i}{b_i S_{mosaic}}\right) = -D.\log(S_{pore}) + Log\ C \quad \text{(Eqn-4)}$$

Where Ni= number of pores with area Spore, bi= bin size, Smosaic= surface area of the current mosaic, C=constant, and D= power-law exponent. The resulting power-law exponent (D) varies between 1.70 to 2.00 (Supplementary data-7).

Effect of texture on porosity, pore morphology, and orientation of pores

We analyzed six samples (SN-7, SN-9, SN-17, SN-28, SN-29 and SN-31) that are enriched in silt content compared to the rest of the mud samples (Supplementary data-7). Silt content has a positive correlation to the total SEM porosity. For example, sample SN-29 (1172.88 mbsf) exhibits a BIB-SEM porosity of 14% whereas other samples from a similar depth with less silt exhibit an average BIB-SEM porosity of 12% (Supplementary data-7) at 20000x magnification. The samples with greater silt content are also enriched in equant-shaped silt-adjacent larger pores (Supplementary data 13a). We also estimated the orientation of the long axis of pores for these three samples and plotted the obtained results as rose diagrams (Supplementary data 13b). The obtained results exhibit a relatively weak preferred alignment of the long axis of pores with respect to the bedding planes (Supplementary data 11b).

Discussions

Effective stress vs porosity: A comparison with experimental study

To understand the consolidation mechanisms of the Sumatra sediment we estimated vertical effective stress following the steps proposed by Hüpers et al., 2015. Following Tarzaghi and Peck (1948) vertical effective stress is expressed as:

$$\sigma_v' = \sigma_v - P_f \quad \text{(Eqn-7)}$$

Here σ_v = total vertical stress caused by the overburden load, and P_f = fluid pressure. To compute vertical effective stress of a layered sediment, we use Eqn 8:

$$\sigma_v' = \sum(\rho_s - \rho_w).\mathbf{g}.\Delta\mathbf{z} \quad \text{(Eqn-8)}$$

where ρ_s= bulk density of the sediment, ρ_w= density of the pore water, Δz= depth interval, and g= gravitational acceleration. During IODP Expedition 362, drilling was performed 255 km away from the deformation front. Although small offset strike-slip faults are evident at the seafloor and in seismic reflection profiles (McNeill et al., 2017), the amount of strain attributed to these fault offsets is compatible with the idea that the maximum horizontal stress is comparable to the vertical stress; there is no evidence in seismic reflection data or from core microstructures for thrust or reverse faults associated with a vertical least principal stress. On this basis, we assume that vertical effective stress is the maximum principal stress. Bulk density of the sediment $\boldsymbol{\rho_s}$ was obtained from McNeill et al., (2017), and $\boldsymbol{\rho_w}$ was considered as the density of sea-water i.e. 1025 kg/m^3 (Hüpers et al., 2015).

We plotted vertical effective stress vs MAD porosity of 55 mud samples (Fig. 10). Fawad et al. (2010) experimentally studied the consolidation behavior of mud with varied proportions of silt and clay. While Sumatra samples follow trends similar to those defined by Fawad et al. (2010), the experimental samples are more compacted than natural Sumatra samples for the same silt content.

Clay mineralogy has a significant effect on the compaction behavior of mudstone (Mondol et al., 2007). Mondol et al. (2007) performed compaction experiments using pure smectite and pure kaolinite clay particle packs; as they represent two end members compared to other clay minerals (illite and chlorite) in terms of grain size and surface area. Smectite is the most fine-grained clay and has the largest surface area; whereas kaolinite is the coarsest one and has smaller surface area among all other clay mineral types (Meade, 1963; Mesri and Olson, 1971; Rieke and Chilingarian, 1974). Hence, kaolinite is more compressible than smectite, and clay compaction gradually decreases with increasing the proportion of small size clay particles in the sample (Mondol et al, 2007).

Fawad et al., (2010) used clay mixtures of 81% kaolinite, 14% mica, and 5% microcline grains, whereas Sumatra mud samples are mainly composed of >73% of illite and lesser smectite, with only <16% undifferentiated chlorite and kaolinite, and <7% quartz particles. Therefore, due to higher illite/smectite content, Sumatra muds appeared to be less compacted compared to the experimental samples used by Fawad et al. (2010).

BIB-SEM porosity vs MAD porosity

We note that BIB-SEM porosity is lower than the porosity found from the shipboard MAD data, however the two measurements correlate along a line through the origin. (Fig.3b). The reason for this difference is that MAD porosity measures the total amount of moisture in a much larger sample and accounts for pores much below the PPR and also rare large pores not included in the 1 mm^2 BIB section. Earlier studies also documented and discussed mismatch between MAD and BIB-SEM measurements (Hemes et al., 2013; Houben et al., 2014; Nole et al., 2016; Olkar et al., 2019). We plotted estimated BIB-SEM porosity and MAD porosity data from earlier studies on BOOM clay (Hemes et a., 2013; Olkar et al., 2019); Opalinus clay (Houben et al., 2014); and samples from Nankai trough (Nole et al., 2016). The data for Boom clay and Opalinus clay follow similar trend as Sumatra samples, whereas clay samples from Nankai trough shows different trend, and it could be attributed due to the difference in magnification of imaging of Nankai samples.

In addition we plotted clay content vs the difference between the two porosities in Supplementary data 14a. We performed regression analysis using the data set for the 33 muds samples analyzed at Aachen (Supplementary data 14b). First, only two variables i.e., BIB-SEM porosity vs MAD porosity (following Eqn-5); second, we considered three variables MAD porosity, BIB-SEM porosity, and clay content (following the Eqn-6).

BIB-SEM porosity=a*MAD porosity + c (Eqn-5)

$$\text{BIB-SEM porosity} = a*\text{MAD porosity} + b*\text{clay content} + c \qquad \text{(Eqn-6)}$$

The coefficient of determinations (R2) for Eqn-5 and Eqn-6 are 0.8408 and 0.9262 respectively. These results show that the ratio in porosity depends on depth and clay content.

For all samples the BIB-SEM pore size distribution follows power-law over an interval of three orders of magnitude. We may extrapolate this below the practical pore resolution (PPR) (Klaver et al., 2012; Kuila and Prasad, 2013; Wang et al., 2019). Extrapolating our data set down to 3nm pore diameter, it is found that BIB-SEM porosity increases only up to 20%~25%. So, there is still an average mismatch of 15% to 20% between the MAD porosity and extrapolated BIB-SEM porosity. The fall off from the normal trend in log-log pore size distribution plots (Fig.9b) for the shallow depth (Unit-I) samples suggest that also large pores are uncounted in the data set. The mud samples from Unit-I contains forams that are rare or absent in the deeper section (Supplementary data-11a, b, c, and d), and missing pore volume can be attributed to the intact forams that may be missed due to the small size of the BIB SEM sample. Moreover, shallow depth samples are richer in smectite compared to the deeper samples, which can also somewhat influence to overestimate the MAD porosity.

Micromechanical model for porosity reduction

Sharp reduction in porosity at the shallow depth from the seafloor to 28 mbsf

High porosity (80% MAD; 32% BIB-SEM) in the shallowest sediments is attributed to large pores in the samples created by abundant EE and EF particle contacts (Fig. 5a and 7a). These contacts are unstable and collapse to form FF contacts, resulting in a rapid porosity decrease with 28m of burial (Table 3). This deformation is apparent from the reduction in large clay domain pores observed over this interval (Fig. 8; Table 2). Collapse of pores surrounded by EE and EF contacts is further recognized by the progressive alignment of clay particles into the bedding plane and by the increase number and consistent orientation of elongated, small, clay domain pores. Each of these observations is consistent with rotation of clay particles into the bedding plane as these large clay domain pores collapse.

Mechanism of porosity reduction from 28 mbsf to 1500 mbsf

Below 28 mbsf to >1500 mbsf, porosity continues to decrease from 50-32% (MAD) but at a reduced pace. SEM observations suggest that this porosity decline results from the progressive loss of silt-adjacent pores with large silt-adjacent pores lost before small ones (Fig. 8), although they remain present in common abundance to1200 mbsf. Small, clay domain pores are abundant throughout the section, and the large clay domain pores were lost above 28 mbsf.

Within the population of silt-adjacent pores, the large, equant pores are most susceptible to collapse (Fig. 8). Large, elongate pores persist in abundance, both in linear and crescent geometries. While it seems plausible that large, equant pores collapse to form large, elongate pores, no corresponding increase in the elongate pore population is observed. Large, elongate pores may collapse further and become small silt-adjacent pores. Microstructural evidence supports the idea that large equant pores collapse as surrounding clay aggregates bend and shrink the size of the remaining pore (Fig. 11a to f), and that the collapse results in an increasing aspect ratio of the pore. While initial pore shrinkage may be accommodated solely by the bending of clay particles above the pore (Fig. 11), further collapse may require clay particles to slide into the pore (Fig.11g-iii) or become fractured (Fig.11g-v) in order to allow clay to invade the pore (model shown in Fig.11 is elaborately described in Supplementary data-15).

Small, silt-adjacent pores also become less abundant with burial, but the transition occurs deeper than the large pores, and small, silt-adjacent pores remain common throughout the section (Fig. 11). Equant, small pores are lost like the large pores, and elongate pores remain abundant within this population subset throughout. There is a loose correspondence between the loss of small, equant pores and an increase in elongate pores, suggesting that pore flattening is part of the pore collapse history. The pore collapse evolution outlined for large pores (Fig. 11) appears to hold for small pores, even though observations are more challenging.

Small, clay domain pores appear to remain resilient throughout the compaction history (Fig. 8), even though some of these pores must become lost to account for porosity loss. Small, equant pores are lost between 100-200 m, and this loss appears to be accommodated by an increase in elongate pores (Fig. 8). Elongate crescent pores increase in abundance around 800 mbsf, and we interpret this to reflect folding of abundant linear elongate pores as the overall system compacts.

Large, equant pores in the clay domain are lost within the first few 10's of meters of burial. Elongate pores appear to form at the expense of equant pores, and there may be a reduction in pore size associated with this shape change. Most of the pores remaining after 1500 m of burial are small, elongate pores found both in clay domain and silt-adjacent pores.

The presence of silt particles locally redistributes the force chain of load to retain silt-adjacent, large pores undeformed (Schneider et al., 2011). The samples with greater silt content are also enriched in equant-shaped silt-adjacent larger pores (Supplementary data 13a) in the microstructure. Hence, and as a result, they display greater porosity compared to other samples from similar depths intervals (Supplementary data-7).

Previous laboratory studies have emphasized the importance of clay particle rotation as a dominant mechanism for mechanical compaction in mudstone (Bennett et al., 1981; Vasseur et al., 1995; Aplin et al., 2006; Day-Stirrat et al., 2008, 2011). While we infer rotation is an important mechanism for mechanical compaction at the shallowest depth where unstable EE and EF particle contacts are present, clay particle bending and sliding/fracturing are considered more important for most of the section studied.

Mechanical compaction of marine sediment: a conceptual model

According to Emmanuel and Day-Stirrat (2020), the reduction of pores in sedimentary rocks during compaction is size-dependent; larger pores deform much readily than smaller pores. According to their model, larger pores rapidly decrease in size during compaction to reduce the overall porosity of the sample. However, microstructural analysis of Sumatra samples suggests that porosity reduction is accomplished by compaction of all pore sizes. While large, clay domain pores are lost more quickly than large, silt-adjacent pores, silt-adjacent pores are larger than clay domain pores. Moreover, the maximum size of pores remains almost constant irrespective of increasing vertical effective stress/depth (Supplementary data 8) with little difference observed for the maximum pore size in samples from 98.25 mbsf and 1299.31 mbsf. The preservation of a constant ratio between MAD and BIB-SEM porosity measurements (Fig. 3b) suggests that porosity loss is distributed across all pore sizes. We infer that all pore sizes are available for compaction for every increment of applied stress but acknowledge that the rate of pore reduction in different size classes may proceed at different rates.

We propose a new model for the reduction in porosity in which all pores within the force chain of load take part in the reduction in porosity during compaction irrespective of their size. At shallow depth up to 28mbsf, larger clay-domain pores are the most susceptible to early response during an increase in compactional strain; because of two reasons- 1) the 'domains' defined by the clay aggregate are weaker compared to the larger rigid silt grains, and 2) due to higher relative proportion of clay-rich regions within the mud, the force chain of load dominantly passes through the clay aggregate. The dispersed nature of the silt-size particles and the high proportion of phyllosilicates in the mud samples indicate that soft clay particles act as the principal load-bearing framework. Hence, larger clay domain pores are more unstable compared to silt adjacent pores in the mud microstructure. Similarly, below 28mbsf depth in Units II and III, under an increase in vertical effective stress, both the larger silt-adjacent pores and smaller pores in the clay matrix that come within the force chain of load collapse. Hence, the ratio between BIB-SEM porosity vs MAD porosity remains almost constant irrespective of the depth. All larger silt-adjacent pores do not come within the force chain of load at the same time. Hence, some of the larger silt-adjacent pores remained undeformed to the maximum depth of 1500mbsf depth. Therefore, the maximum size of the larger silt adjacent larger pores remains almost constant irrespective of the depth/vertical effective stress.

While our understanding of how different pore types is consistent with all available data, tracking the pore evolution through additional size categories would elucidate the pore evolution in more detail. Preliminary pore size distribution data (Fig.9) indicate that 4 size bins exist in these samples. Developing this approach requires improved image analysis techniques to tie all the pore attributes together on a pore-by-pore basis for a huge number of pores.

Compaction strain accommodation and grain-scale deformation

Deformation of clay-rich sedimentary rocks involves four possible mechanisms: 1) Particulate flow; (Morgenstern and Tchalenko, 1967; Borradaile et al., 1981); 2) Cataclasis; (Ukar and Cloos, 2019) 3) Diffusive mass transfer; (Blenkinsop, 2000; Fossen, 2016); 4) Intercrystalline plasticity (Blenkinsop, 2000; Fossen, 2016). The intensity and occurrence of a particular deformation mechanism in mudstone depend on several parameters, such as effective stress, water content, cementation, temperature (Desbois et al., 2017; Den Hartog and Spiers, 2014).

All our samples show evidence of particulate flow controlled by friction between grains. At shallow depths, illite platelets contacted at EE and EF junctions lose these weak bonds, and particles rotate into bedding-parallel orientation. Once FF contacts dominate, large-scale rotations are reduced and intra-crystalline slip becomes important. This is best evidenced in collapse of large, silt-adjacent pores where bent clay particles overlie pores (Fig.11). In deforming granular foam material, bending was reported as the dominant deformation mechanism for the reduction in porosity and developing preferred alignment of the long axis of pores perpendicular to the applied stress (Elliott et al., 2002; Zhou et al., 2004; Samsudin et al., 2017; Zakaria et al., 2018) (review of these earlier studies on the experimental deformation of granular foam is described in supplementary data-16). Friction adheres clay particles to the edge of pores while the middle of particles drops into the pore, resulting in bending by intra-crystalline slip. A cartoon (Fig. 12g) illustrates the compaction mechanism associated with the bending of clay particles. With increasing compaction strain, clay particles undergo bending, and as a result, pore area reduces and the orientation of the pores tends to align perpendicular to the applied effective stress (Fig. 12g).

Compaction of Sumatra input section: generalized implication for rock property evolution

The overall compaction curve obtained for Sumatra muds is comparable with the experimental study by Fawad et al., 2010 in the context of compactional range (Fig. 8). The curve shows a monoexponential decrease in porosity with an increase in vertical effective stress, which is evidence of normal consolidation (Fawad et al., 2010; Dutilleul et al., 2020).

The larger silt-adjacent pores seen in the deepest of these samples (1500 m burial) suggest these muds retain considerable potential for additional compaction in deeper burial. As this marine sediment progressively approaches greater burial at closer proximity of the accretionary prism, it will undergo further change in physical and deformational properties (Bray and Karig, 1985). Despite the substantial compactional strain, the relatively high porosity of the deepest sample and the survival of larger and mechanically unstable silt-margin pores suggests that compactional stabilization has not been reached because such IGVs and pore types are not generally observed in older and lithified mudrocks. Based on the current understanding of subduction zone deformation behavior and mudrock properties, it seems likely that compaction will continue to dominate the pore loss in deeper burial.

The general absence of early cementation and the corresponding dominance of compaction in the total pore loss, is consistent with observations of other siliciclastic-dominated muds (Milliken, 2014; 2019). The trends for intergranular volume observed across the seafloor to 1500mbsf place useful constraints on the maximum cement volumes that theoretically could be emplaced at this depth range in sediments containing a more reactive grain assemblage. At the depths of burial attained at the deformation front, any cementation of the Sumatra input sediments will be limited to <30% of the rock volume, or possibly much less, as compaction is expected to continue up to the burial temperatures that initiate grain reactions and associated cementation.

Conclusions

Pores can be classified by size and also microstructural position. Their contribution to the total porosity is multimodal.

Samples at shallow depth (seafloor to 28 mbsf) display a sharp reduction in porosity from 80% to 52% due to the collapse of the large clay domain/matrix pores. Deeper samples (28 mbsf to 1500 mbsf) exhibit a smaller reduction in porosity from 50% to 32% due to collapse of silt-adjacent pores by bending and subsequently fracturing/sliding of clay aggregate.

Large equant pores in clay (between 10^6 and 10^7 nm^2) are rare below the first few meters of burial, after the flocculated structure collapses.

This hasn't really been discussed until here. Put a paragraph in the discussion with appropriate references

The class of large pores next to silt-size grains (between 10^4 and 10^6 nm^2) remains common to >1 km burial, irrespective of the mineralogy of the silt-sized grains, but their size decreases with depth. Small, equant pores next to silt particles are abundant in the first 100 m of burial and remain common over the whole samples depth range.

Small pores in clay domains are almost all elongated, and abundant over all observed depths. Small, crescent-shaped elongate pores increase in abundance with depth as clay particles become folded by compactional processes.

The size-independence of pore loss arises because the force chain driving pore collapse is localized primarily within the volumetrically dominant and weaker clay-rich domains; larger pores around isolated silt particles enter into the force chain somewhat randomly and asynchronously and do not contribute preferentially to pore loss over the depth range studied.

An increase in effective stress up to 18MPa (~1500 mbsf) causes the development of weakly aligned phyllosilicate fabric (defined by mica and illite clay particles) in the microstructure.

Compaction processes in our samples are dominated by granular flow (rotation and frictional sliding of illite clay particles) at shallow depths. With increasing depth, compaction is additionally accommodated by bending of clay particles.

Data availability

High resolution SE2 and BSE images of all samples are available online at:
https://figshare.com/s/cbaada517b0b1409d575

Authors contributions

SL and KLM performed sample preparation and BIB-SEM microscopy. SL analysed the data. JLU and GD acquired funding. JLU managed the project. PV, KLM and JLU significantly contributed to interpret the data. SL wrote the first draft of the manuscript. PV, KLM and JLU contributed for the correction and improvement of the manuscript.

Competing interests

The authors declare that they do not have any conflict of interest.

Acknowledgments

SL and JLU thank German Research Foundation (Deutsche Forschungsgemeinschaft [DFG] grant UR 64/19-1) for providing funding to carry out the research. IODP (International Ocean Discovery Programme) sample repository, Japan is acknowledged for providing oriented mud samples for the study. KLM acknowledges the samples and data provided by the International Ocean Discovery Program (IODP). Funding for sample preparation and SEM imaging was supported by a post-expedition award (Milliken, P.I.) from the Consortium for Ocean Leadership. SL thanks Manuel Menzel, Jop Klaver, Liene Spruženiece, and Joyce Schmatz for providing valuable time to teach BIB-SEM techniques.

References

Ajdukiewicz, J. M. and R. H. Lander 2010. Sandstone reservoir quality prediction: state of the art. AAPG Bulletin 94: 1082-1091.

Alam, M., Alam, M.M., Curray, J.R., Chowdhury, M.L.R. and Gani, M.R., 2003. An overview of the sedimentary geology of the Bengal Basin in relation to the regional tectonic framework and basin-fill history. Sedimentary geology, 155(3-4), pp.179-208.

Al-Mukhtar, M., Belanteur, N., Tessier, D., and Vanapalli, S.K. (1996). The fabric of a clay soil under controlled mechanical and hydraulic stress states. Appl. Clay Sci. 11, 99–115.

Ammon, C.J., Ji, C., Thio, H.K., Robinson, D., Ni, S., Hjorleifsdottir, V., Kanamori, H., Lay, T., Das, S., Helmberger, D. and Ichinose, G., 2005. Rupture process of the 2004 Sumatra-Andaman earthquake. science, 308(5725), pp.1133-1139.

Aplin, A. C., I. F. Matenaar, D. K. McCarty and B. A. van der Pluijm 2006. Influence of mechanical compaction and clay mineral diagenesis on the microfabric and pore-scale properties of deep-water Gulf of Mexico mudstones. Clays and Clay Minerals 54: 514-500.

Aplin, A.C. and Yagiz, J.H., 2011. Mudstone diversity: Origin and implications for source, seal, and reservoir properties in petroleum systems. AAPG bulletin, 95(12), pp.2031-2059.

Aplin, A.C., Matenaar, I.F. and van der Pluijm, B., 2003. Influence of mechanical compaction and chemical diagenesis on the microfabric and fluid flow properties of Gulf of Mexico mudstones. Journal of Geochemical Exploration, 78, pp.449-451.

Aplin, A.C., Matenaar, I.F., McCarty, D.K. and van Der Pluijm, B.A., 2006. Influence of mechanical compaction and clay mineral diagenesis on the microfabric and pore-scale properties of deep-water Gulf of Mexico mudstones. Clays and Clay Minerals, 54(4), pp.500-514.

Backman, J., W. Chen, S. Kachovich, F. L. Mitchison, K. E. Petronotis, T. Yang and X. Zhao (2019). Data report; Revised age models for IODP Sites U1480 and U1481, Expedition 362. Proceedings of the International Ocean Discovery Program, Expedition Reports 362: 7.

Bennett, R.H., Bryant, W.R. and Keller, G.H., 1981. Clay fabric of selected submarine sediments; fundamental properties and models. Journal of Sedimentary Research, 51(1), pp.217-232.

Bennett, R.H., O'Brien, N.R. and Hulbert, M.H., 1991. Determinants of clay and shale microfabric signatures: processes and mechanisms. In Microstructure of Fine-Grained Sediments (pp. 5-32). Springer, New York, NY.

Bjørlykke, K. and Høeg, K., 1997. Effects of burial diagenesis on stresses, compaction and fluid flow in sedimentary basins. Marine and Petroleum Geology, 14(3), pp.267-276.

Bjørlykke, K., 1998. Clay mineral diagenesis in sedimentary basins-a key to the prediction of rock properties. Examples from the North Sea Basin. Clay minerals, 33(1), pp.15-34.

Blenkinsop, T.G., 2007. Deformation microstructures and mechanisms in minerals and rocks. Springer Science & Business Media.

Boisson, J.Y. (2005). Clay Club Catalogue of Characteristics of Argillaceous Rocks (OECD NEA No. 4436).

Borradaile, G.J., 1981. Particulate flow of rock and the formation of cleavage. Tectonophysics, 72(3-4), pp.305-321.

Bowles, F.A., Bryant, W.R. and Wallin, C., 1969. Microstructure of unconsolidated and consolidated marine sediments. Journal of Sedimentary Research, 39(4), pp.1546-1551.

Bray, C.J. and Karig, D.E., 1985. Porosity of sediments in accretionary prisms and some implications for dewatering processes. Journal of Geophysical Research: Solid Earth, 90(B1), pp.768-778.

Casagrande, A., 1932. Research on the Atterberg limits of soils. Public roads, 13(8), pp.121-136.

Casagrande, A., 1932. The structure of clay and its importance in foundation engineering. Boston Society Civil Engineers Journal.

Cetin, H., 2004. Soil-particle and pore orientations during consolidation of cohesive soils. Engineering geology, 73(1-2), pp.1-11.

Chester, F.M., Rowe, C., Ujiie, K., Kirkpatrick, J., Regalla, C., Remitti, F., Moore, J.C., Toy, V., Wolfson-Schwehr, M., Bose, S. and Kameda, J., 2013. Structure and composition of the plate-boundary slip zone for the 2011 Tohoku-Oki earthquake. Science, 342(6163), pp.1208-1211.

Collins, K.T. and McGown, A., 1974. The form and function of microfabric features in a variety of natural soils. Geotechnique, 24(2), pp.223-254.

Cook, B.J., Henstock, T.J., McNeill, L.C. and Bull, J.M., 2014. Controls on spatial and temporal evolution of prism faulting and relationships to plate boundary slip offshore north-central Sumatra. Journal of Geophysical Research: Solid Earth, 119(7), pp.5594-5612.

Cubas, N., Souloumiac, P. and Singh, S.C., 2016. Relationship link between landward vergence in accretionary prisms and tsunami generation. Geology, 44(10), pp.787-790.

Curtis, C.D., Lipshie, S.R., Oertel, G. and Pearson, M.J., 1980. Clay orientation in some Upper Carboniferous mudrocks, its relationship to quartz content and some inferences about fissility, porosity and compactional history. Sedimentology, 27(3), pp.333-339.

Day-Stirrat, R.J., Aplin, A.C., Środoń, J. and Van der Pluijm, B.A., 2008. Diagenetic reorientation of phyllosilicate minerals in Paleogene mudstones of the Podhale Basin, southern Poland. Clays and Clay Minerals, 56(1), pp.100-111.

Day-Stirrat, R.J., Flemings, P.B., You, Y., Aplin, A.C. and van der Pluijm, B.A., 2012. The fabric of consolidation in Gulf of Mexico mudstones. Marine Geology, 295, pp.77-85.

Day-Stirrat, R.J., Milliken, K.L., Dutton, S.P., Loucks, R.G., Hillier, S., Aplin, A.C. and Schleicher, A.M., 2010. Open-system chemical behavior in deep Wilcox Group mudstones, Texas Gulf Coast, USA. Marine and Petroleum Geology, 27(9), pp.1804-1818.

Dean, S.M., McNeill, L.C., Henstock, T.J., Bull, J.M., Gulick, S.P., Austin, J.A., Bangs, N.L., Djajadihardja, Y.S. and Permana, H., 2010. Contrasting décollement and prism properties over the Sumatra 2004–2005 earthquake rupture boundary. Science, 329(5988), pp.207-210.

Den H, S.A. and Spiers, C.J., 2014. A microphysical model for fault gouge friction applied to subduction megathrusts. Journal of Geophysical Research: Solid Earth, 119(2), pp.1510-1529.

Desbois, G., Höhne, N., Urai, J.L., Bésuelle, P. and Viggiani, G., 2017. Deformation in cemented mudrock (Callovo–Oxfordian Clay) by microcracking, granular flow and phyllosilicate plasticity: insights from triaxial deformation, broad ion beam polishing and scanning electron microscopy. Solid Earth, 8(2), pp.291-305.

Desbois, G., Urai, J.L. and Kukla, P.A., 2009a. Morphology of the pore space in claystones–evidence from BIB/FIB ion beam sectioning and cryo-SEM observations. eEarth Discussions, 4(1), pp.1-19.

Desbois, G., Urai, J.L., Kukla, P.A., Konstanty, J. and Baerle, C., 2011. High-resolution 3D fabric and porosity model in a tight gas sandstone reservoir: A new approach to investigate microstructures from mm-to nm-scale combining argon beam cross-sectioning and SEM imaging. Journal of Petroleum Science and Engineering, 78(2), pp.243-257.

Backman, J., W. Chen, S. Kachovich, F. L. Mitchison, K. E. Petronotis, T. Yang and X. Zhao (2019). Data report; Revised age models for IODP Sites U1480 and U1481, Expedition 362. Proceedings of the International Ocean Discovery Program, Expedition Reports 362: 7.

Bennett, R.H., Bryant, W.R. and Keller, G.H., 1981. Clay fabric of selected submarine sediments; fundamental properties and models. Journal of Sedimentary Research, 51(1), pp.217-232.

Bennett, R.H., O'Brien, N.R. and Hulbert, M.H., 1991. Determinants of clay and shale microfabric signatures: processes and mechanisms. In Microstructure of Fine-Grained Sediments (pp. 5-32). Springer, New York, NY.

Bjørlykke, K. and Høeg, K., 1997. Effects of burial diagenesis on stresses, compaction and fluid flow in sedimentary basins. Marine and Petroleum Geology, 14(3), pp.267-276.

Bjørlykke, K., 1998. Clay mineral diagenesis in sedimentary basins-a key to the prediction of rock properties. Examples from the North Sea Basin. Clay minerals, 33(1), pp.15-34.

Blenkinsop, T.G., 2007. Deformation microstructures and mechanisms in minerals and rocks. Springer Science & Business Media.

Boisson, J.Y. (2005). Clay Club Catalogue of Characteristics of Argillaceous Rocks (OECD NEA No. 4436).

Borradaile, G.J., 1981. Particulate flow of rock and the formation of cleavage. Tectonophysics, 72(3-4), pp.305-321.

Bowles, F.A., Bryant, W.R. and Wallin, C., 1969. Microstructure of unconsolidated and consolidated marine sediments. Journal of Sedimentary Research, 39(4), pp.1546-1551.

Bray, C.J. and Karig, D.E., 1985. Porosity of sediments in accretionary prisms and some implications for dewatering processes. Journal of Geophysical Research: Solid Earth, 90(B1), pp.768-778.

Casagrande, A., 1932. Research on the Atterberg limits of soils. Public roads, 13(8), pp.121-136.

Casagrande, A., 1932. The structure of clay and its importance in foundation engineering. Boston Society Civil Engineers Journal.

Cetin, H., 2004. Soil-particle and pore orientations during consolidation of cohesive soils. Engineering geology, 73(1-2), pp.1-11.

Chester, F.M., Rowe, C., Ujiie, K., Kirkpatrick, J., Regalla, C., Remitti, F., Moore, J.C., Toy, V., Wolfson-Schwehr, M., Bose, S. and Kameda, J., 2013. Structure and composition of the plate-boundary slip zone for the 2011 Tohoku-Oki earthquake. Science, 342(6163), pp.1208-1211.

Desbois, G., Urai, J.L. and Kukla, P.A., 2009b. Morphology of the pore space in claystones–evidence from BIB/FIB ion beam sectioning and cryo-SEM observations. eEarth Discussions, 4(1), pp.1-19.

Desbois, G., Urai, J.L., Hemes, S., Brassinnes, S., De Craen, M. and Sillen, X., 2014. Nanometer-scale pore fluid distribution and drying damage in preserved clay cores from Belgian clay formations inferred by BIB-cryo-SEM. Engineering Geology, 179, pp.117-131.

Desbois, G., Urai, J.L., Hemes, S., Brassinnes, S., De Craen, M. and Sillen, X., 2014. Nanometer-scale pore fluid distribution and drying damage in preserved clay cores from Belgian clay formations inferred by BIB-cryo-SEM. Engineering Geology, 179, pp.117-131.

Díaz-Azpiroz, M., Brune, S., Leever, K.A., Fernández, C. and Czeck, D.M., 2016. Tectonics of oblique plate boundary systems. Tectonophysics, 693, pp.165-170.

Djéran-Maigre, I., Tessier, D., Grunberger, D., Velde, B. and Vasseur, G., 1998. Evolution of microstructures and of macroscopic properties of some clays during experimental compaction. Marine and Petroleum Geology, 15(2), pp.109-128.

Djéran-Maigre, I., Tessier, D., Grunberger, D., Velde, B. and Vasseur, G., 1998. Evolution of microstructures and of macroscopic properties of some clays during experimental compaction. Marine and Petroleum Geology, 15(2), pp.109-128.

Dugan, B., McNeill, L. and Petronotis, K., 2017. Expedition 362 preliminary report: Sumatra subduction zone. International Ocean Discovery Program.

Dutilleul, J., Bourlange, S., Conin, M. and Géraud, Y., 2020. Quantification of bound water content, interstitial porosity and fracture porosity in the sediments entering the North Sumatra subduction zone from Cation Exchange Capacity and IODP Expedition 362 resistivity data. Marine and Petroleum Geology, 111, pp.156-165.

Dutta, N.C., 1986. Shale compaction, burial diagenesis, and geopressures: A dynamic model, solution and some results. Collection colloques et séminaires-Institut français du pétrole, (44), pp.149-172.

Ehrenberg, S. N. 1989. Assessing the relative importance of compaction processes and cementation to reduction of porosity in sandstones: discussion. American Association of Petroleum Geologists Bulletin 73: 1274-1276.

Emmanuel, S. and Day-Stirrat, R.J., 2012. A framework for quantifying size dependent deformation of nano-scale pores in mudrocks. Journal of applied geophysics, 86, pp.29-35.

Fawad, M., Mondol, N.H., Jahren, J. and Bjørlykke, K., 2010. Microfabric and rock properties of experimentally compressed silt-clay mixtures. Marine and Petroleum Geology, 27(8), pp.1698-1712.

Fernandez-Blanco, D., Philippon, M. and von Hagke, C., 2016. Structure and kinematics of the Sumatran fault system in North Sumatra (Indonesia). Tectonophysics, 693, pp.453-464.

Fossen, H., 2016. Structural geology. Cambridge university press.

Geersen, J., McNeill, L., Henstock, T.J. and Gaedicke, C., 2013. The 2004 Aceh-Andaman Earthquake: Early clay dehydration controls shallow seismic rupture. Geochemistry, Geophysics, Geosystems, 14(9), pp.3315-3323.

Ghosal, D., Singh, S.C. and Martin, J., 2014. Shallow subsurface morphotectonics of the NW Sumatra subduction system using an integrated seismic imaging technique. Geophysical Journal International, 198(3), pp.1818-1831.

Gulick, S.P., Austin, J.A., McNeill, L.C., Bangs, N.L., Martin, K.M., Henstock, T.J., Bull, J.M., Dean, S., Djajadihardja, Y.S. and Permana, H., 2011. Updip rupture of the 2004 Sumatra earthquake extended by thick indurated sediments. Nature Geoscience, 4(7), pp.453-456.

Guo, P. and Stolle, D.F.E., 2013. Coupled analysis of bifurcation and shear band in saturated soils. Soils and foundations, 53(4), pp.525-539.

Handy, M.R., 1994. Flow laws for rocks containing two non-linear viscous phases: a phenomenological approach. Journal of Structural Geology, 16(3), pp.287-301.

Hemes, S., Desbois, G., Klaver, J. and Urai, J.L., 2016. Microstructural characterisation of the Ypresian clays (Kallo-1) at nanometre resolution, using broad-ion beam milling and scanning electron microscopy. Netherlands Journal of Geosciences, 95(3), pp.293-313.

Hemes, S., Desbois, G., Urai, J.L., De Craen, M. and Honty, M., 2013. Variations in the morphology of porosity in the Boom Clay Formation: insights from 2D high resolution BIB-SEM imaging and Mercury injection Porosimetry. Netherlands Journal of geosciences, 92(4), pp.275-300.

Hemes, S., Desbois, G., Urai, J.L., De Craen, M. and Honty, M., 2013. Variations in the morphology of porosity in the Boom Clay Formation: insights from 2D high resolution BIB-SEM imaging and Mercury injection Porosimetry. Netherlands Journal of geosciences, 92(4), pp.275-300.

Hemes, S., Desbois, G., Urai, J.L., Schröppel, B. and Schwarz, J.O., 2015. Multi-scale characterization of porosity in Boom Clay (HADES-level, Mol, Belgium) using a combination of X-ray μ-CT, 2D BIB-SEM and FIB-SEM tomography. Microporous and mesoporous materials, 208, pp.1-20.

Hesse, R., 1975. Turbiditic and non-turbiditic mudstone of Cretaceous flysch sections of the East Alps and other basins. Sedimentology, 22(3), pp.387-416.

Hippchen, S. and Hyndman, R.D., 2008. Thermal and structural models of the Sumatra subduction zone: Implications for the megathrust seismogenic zone. Journal of Geophysical Research: Solid Earth, 113(B12).

Ho, N.C., Peacor, D.R. and Van der Pluijm, B.A., 1999. Preferred orientation of phyllosilicates in Gulf Coast mudstones and relation to the smectite-illite transition. Clays and Clay Minerals, 47(4), pp.495-504.

Houben, M.E., Desbois, G. and Urai, J.L., 2013. Pore morphology and distribution in the Shaly facies of Opalinus Clay (Mont Terri, Switzerland): Insights from representative 2D BIB–SEM investigations on mm to nm scale. Applied Clay Science, 71, pp.82-97.

Houben, M.E., Desbois, G. and Urai, J.L., 2014. A comparative study of representative 2D microstructures in Shaly and Sandy facies of Opalinus Clay (Mont Terri, Switzerland) inferred form BIB-SEM and MIP methods. Marine and Petroleum Geology, 49, pp.143-161.

Hunze, S. and Wonik, T., 2007. Compaction in the Nankai and Barbados accretionary prisms: New insights from logging-while-drilling data. Geochemistry, Geophysics, Geosystems, 8(2).

Hüpers, A., Ikari, M.J., Dugan, B., Underwood, M.B. and Kopf, A.J., 2015. Origin of a zone of anomalously high porosity in the subduction inputs to Nankai Trough. Marine Geology, 361, pp.147-162.

Hüpers, A., Torres, M.E., Owari, S., McNeill, L.C., Dugan, B., Henstock, T.J., Milliken, K.L., Petronotis, K.E., Backman, J., Bourlange, S. and Chemale, F., 2017. Release of mineral-bound water prior to subduction tied to shallow seismogenic slip off Sumatra. Science, 356(6340), pp.841-844.

Ikari, M.J., Niemeijer, A.R. and Marone, C., 2015. Experimental investigation of incipient shear failure in foliated rock. Journal of Structural Geology, 77, pp.82-91.

Illangasekare, T., Tyler, S.W., Clement, T.P., Villholth, K.G., Perera, A.P.G.R.L., Obeysekera, J., Gunatilaka, A., Panabokke, C.R., Hyndman, D.W., Cunningham, K.J. and Kaluarachchi, J.J., 2006. Impacts of the 2004 tsunami on groundwater resources in Sri Lanka. Water Resources Research, 42(5).

Ingram, G.M. and Urai, J.L., 1999. Top-seal leakage through faults and fractures: the role of mudrock properties. Geological Society, London, Special Publications, 158(1), pp.125-135.

Jacob, G., Kisch, H.J. and van der Pluijm, B.A., 2000. The relationship of phyllosilicate orientation, X-ray diffraction intensity ratios, and c/b fissility ratios in metasedimentary rocks of the Helvetic zone of the Swiss Alps and the Caledonides of Jaemtland, central western Sweden. Journal of Structural Geology, 22(2), pp.245-258.

Jessell, M.W., Bons, P.D., Griera, A., Evans, L.A. and Wilson, C.J., 2009. A tale of two viscosities. Journal of Structural Geology, 31(7), pp.719-736.

Jiang, M., Klaver, J., Schmatz, J. and Urai, J.L., 2015. Nanoscale porosity analysis in geological materials. Acta Stereologica.

Kameda, A., Dvorkin, J., Keehm, Y., Nur, A. and Bosl, W., 2006. Permeability-porosity transforms from small sandstone fragments. Geophysics, 71(1), pp.N11-N19.

Karaborni, S., Smit, B., Heidug, W., Urai, J. and Van Oort, E., 1996. The swelling of clays: molecular simulations of the hydration of montmorillonite. Science, 271(5252), pp.1102-1104.

Klaver, J., Desbois, G., Littke, R. and Urai, J.L., 2015. BIB-SEM characterization of pore space morphology and distribution in postmature to overmature samples from the Haynesville and Bossier Shales. Marine and petroleum Geology, 59, pp.451-466.

Klaver, J., Desbois, G., Littke, R. and Urai, J.L., 2016. BIB-SEM pore characterization of mature and post mature Posidonia Shale samples from the Hils area, Germany. International Journal of Coal Geology, 158, pp.78-89.

Klaver, J., Desbois, G., Urai, J.L. and Littke, R., 2012. BIB-SEM study of the pore space morphology in early mature Posidonia Shale from the Hils area, Germany. International Journal of Coal Geology, 103, pp.12-25.

Klaver, J., Desbois, G., Urai, J.L. and Littke, R., 2012. BIB-SEM study of the pore space morphology in early mature Posidonia Shale from the Hils area, Germany. International Journal of Coal Geology, 103, pp.12-25.

Klaver, J., Hemes, S., Houben, M., Desbois, G., Radi, Z. and Urai, J.L., 2015. The connectivity of pore space in mudstones: insights from high-pressure Wood's metal injection, BIB-SEM imaging, and mercury intrusion porosimetry. Geofluids, 15(4), pp.577-591.

Klaver, J., Hemes, S., Houben, M., Desbois, G., Radi, Z. and Urai, J.L., 2015. The connectivity of pore space in mudstones: insights from high-pressure Wood's metal injection, BIB-SEM imaging, and mercury intrusion porosimetry. Geofluids, 15(4), pp.577-591.

Klinkenberg, M., Kaufhold, S., Dohrmann, R. and Siegesmund, S., 2009. Influence of carbonate microfabrics on the failure strength of claystones. Engineering Geology, 107(1-2), pp.42-54.

Kooi, H., 1997. Insufficiency of compaction disequilibrium as the sole cause of high pore fluid pressures in pre-Cenozoic sediments. Basin Research, 9(3), pp.227-241.

Kuila, U. and Prasad, M., 2013. Specific surface area and pore-size distribution in clays and shales. Geophysical Prospecting, 61(2-Rock Physics for Reservoir Exploration, Characterisation and Monitoring), pp.341-362.

Kuncoro, A.K., Cubas, N., Singh, S.C., Etchebes, M. and Tapponnier, P., 2015. Tsunamigenic potential due to frontal rupturing in the Sumatra locked zone. Earth and Planetary Science Letters, 432, pp.311-322.

Lahann, R., Huffman, A.R. and Bowers, G.L., 2002. Impact of smectite diagenesis on compaction modeling and compaction equilibrium. MEMOIRS-AMERICAN ASSOCIATION OF PETROLEUM GEOLOGISTS, pp.61-72.

Lambe, T.W., 1953, October. The structure of inorganic soil. In Proceedings of the American Society of Civil Engineers (Vol. 79, No. 10, pp. 1-49). ASCE.

Lambe, T.W., 1958. The structure of compacted clays. Journal of the Soil Mechanics and Foundations Division, 84(2), pp.1654-1.

Lander, R. H. and O. Walderhaug 1999. Predicting porosity through simulating sandstone compaction and quartz cementation. American Association of Petroleum Geologists Bulletin 83: 433-449.

Lander, R. H., R. H. Larese and L. M. Bonnell 2008. Toward more accurate quartz cement models: The importance of euhedral versus noneuhedral growth rates. American Association Petroleum Geologists Bulletin 92: 1537-1563.

Laurich, B., Urai, J.L. and Nussbaum, C., 2017. Microstructures and deformation mechanisms in Opalinus Clay: Insights from scaly clay from the Main Fault in the Mont Terri Rock Laboratory (CH). Solid Earth, 8(1), pp.27-44.

Laurich, B., Urai, J.L., Desbois, G., Vollmer, C. and Nussbaum, C., 2014. Microstructural evolution of an incipient fault zone in Opalinus Clay: Insights from an optical and electron microscopic study of ion-beam polished samples from the Main Fault in the Mt-Terri Underground Research Laboratory. Journal of Structural Geology, 67, pp.107-128.

Lay, T., Ammon, C.J., Kanamori, H., Yamazaki, Y., Cheung, K.F. and Hutko, A.R., 2011. The 25 October 2010 Mentawai tsunami earthquake (Mw 7.8) and the tsunami hazard presented by shallow megathrust ruptures. Geophysical Research Letters, 38(6).

Lay, T., Kanamori, H., Ammon, C.J., Nettles, M., Ward, S.N., Aster, R.C., Beck, S.L., Bilek, S.L., Brudzinski, M.R., Butler, R. and DeShon, H.R., 2005. The great Sumatra-Andaman earthquake of 26 december 2004. science, 308(5725), pp.1127-1133.

Lazar, O.R., Bohacs, K.M., Macquaker, J.H., Schieber, J. and Demko, T.M., 2015. Capturing key attributes of fine-grained sedimentary rocks in outcrops, cores, and thin sections: nomenclature and description guidelines. Journal of Sedimentary Research, 85(3), pp.230-246.

Li, Z. and J. Schieber 2018. Composite particles in mudstones: Examples from the Late Cretaceous Tununk shale member of the Mancos Shale Formation. Journal of Sedimentary Research 8812: 1319-1344. Lithic grains in shale

Li, Z., J. Schieber and P. K. Pedersen 2021. On the origin and significance of composite particles in mudstones; examples from the Cenomanian Dunvegan Formation. Sedimentology 682: 737-754. Lithic grains in shale

Logan, J.M. and Rauenzahn, K.A., 1987. Frictional dependence of gouge mixtures of quartz and montmorillonite on velocity, composition and fabric. Tectonophysics, 144(1-3), pp.87-108.

Lu, J., K. L. Milliken and R. M. Reed 2011. Diagenesis and sealing capacity of the Middle Tuscaloosa mudstone at the Cranfield CO2 injection site, Mississippi, USA. Environmental Geosciences 3: 35-53.

Lundegard, P. D. 1992. Sandstone porosity loss--a 'big picture' view of the importance of compaction. Journal of Sedimentary Petrology 62: 250-260.

Lupini, J.F., Skinner, A.E. and Vaughan, P.R., 1981. The drained residual strength of cohesive soils. Geotechnique, 31(2), pp.181-213.

Mandelbrot, B.B., Pfeifer, P., Biham, O., Malcai, O., Lidar, D. and Avnir, D., 1998. Is nature fractal?. Science, 279(5352), pp.783-783.

March, A., 1932. Mathematische Theorie der Regelung nach der Korngestalt bei affiner Deformation: Zeitschrift fur Kristallographie, v. 81.

McNeill, L.C. and Henstock, T.J., 2014. Forearc structure and morphology along the Sumatra-Andaman subduction zone. Tectonics, 33(2), pp.112-134.

McNeill, L.C., Dugan, B. and Petronotis, K.E., The Expedition 362 Scientists (2017). Sumatra Subduction Zone. Proceedings of the International Ocean Discovery Program, 362.

Meade, R.H., 1964. Removal of water and rearrangement of particles during the compaction of clayey sediments. US Government Printing Office.

Miller, S.A., 2013. The role of fluids in tectonic and earthquake processes. In Advances in geophysics (Vol. 54, pp. 1-46). Elsevier.

Milliken K. L. 2019. Compactional and mass-balance constraints inferred from the volume of quartz cementation in mudrocks. Mudstone Diagenesis: New Research Perspectives for Shale Hydrocarbon Reservoirs, Seals, and Source Rocks. AAPG. 120: 33-48.

Milliken, K. L. 2014. A compositional classification for grain assemblages in fine-grained sediments and sedimentary rocks. Journal of Sedimentary Research 84: 1185-1199.

check date P2, L66

Milliken, K. L. and M. E. Curtis 2016. Imaging pores in sedimentary rocks: Foundation of porosity prediction. Marine and Petroleum Geology 73: 590-608.

Milliken, K. L. and R. J. Day-Stirrat 2013. Cementation in mudrocks: Brief review with examples from cratonic basin mudrocks. Memoir. J.-Y. Chatellier. Tulsa, Oklahoma, USA, AAPG: in press.

Milliken, K. L. and T. Olson 2017. Silica diagenesis, porosity evolution, and mechanical behavior in siliceous mudstones, Mowry Shale Cretaceous, Rocky Mountains, U.S.A. Journal of Sedimentary Research 87: 366-387.

Milliken, K. L., M. Rudnicki, D. N. Awwiller and T. Zhang 2013. Organic matter-hosted pore system, Marcellus Formation Devonian, Pennsylvania, USA. AAPG Bulletin 97: 177-200.

Milliken, K. L., W. L. Esch, R. M. Reed and T. Zhang 2012. Grain assemblages and strong diagenetic overprinting in siliceous mudrocks, Barnett Shale Mississippian, Fort Worth Basin, Texas, U.S.A. AAPG Bulletin 96: 1553-1578.

Milliken, K., and Olson, T., 2016, Amorphous and crystalline solids as artifacts in SEM images, in Olson, T., Imaging Unconventional Reservoir Pore Systems: AAPG Memoir, v. 112, p. 1-8, http://doi.org/10.1306/13592013M112252.

Milliken, K.L. and Hayman, N.W., 2019. Mudrock components and the genesis of bulk rock properties: review of current advances and challenges. Shale: Subsurface Science and Engineering, pp.1-25.

Mitchell, J.K., 1956. The fabric of natural clays and its relation to engineering properties. In Highway Research Board Proceedings (Vol. 35).

Moeremans, R., Singh, S.C., Mukti, M., McArdle, J. and Johansen, K., 2014. Seismic images of structural variations along the deformation front of the Andaman–Sumatra subduction zone: implications for rupture propagation and tsunamigenesis. Earth and Planetary Science Letters, 386, pp.75-85.

Moeremans, R.E. and Singh, S.C., 2014. Seismic evidence of continental margin influence on the NinetyEast Ridge in the Bay of Bengal. Geophysical Research Letters, 41(20), pp.7143-7150.

Moeremans, R.E. and Singh, S.C., 2015. Fore-arc basin deformation in the Andaman-Nicobar segment of the Sumatra-Andaman subduction zone: Insight from high-resolution seismic reflection data. Tectonics, 34(8), pp.1736-1750.

Mondol, N.H., Bjørlykke, K., Jahren, J. and Høeg, K., 2007. Experimental mechanical compaction of clay mineral aggregates—Changes in physical properties of mudstones during burial. Marine and petroleum geology, 24(5), pp.289-311.

Moon, C.F., 1972. The microstructure of clay sediments. Earth-Science Reviews, 8(3), pp.303-321.

Moore, D.E. and Lockner, D.A., 2004. Crystallographic controls on the frictional behavior of dry and water-saturated sheet structure minerals. Journal of Geophysical Research: Solid Earth, 109(B3).

Moore, D. M. and R. C. Reynolds, Jr. (1989). X-ray diffraction and the identification and analysis of clay minerals. United States, Oxford Univ. Press : New York, NY, 332 p.Morgenstern, N.R. and Tchalenko, J.S., 1967. Microscopic structures in kaolin subjected to direct shear. Geotechnique, 17(4), pp.309-328.

Morgenstern, N.R. and Tchalenko, J.S., 1967. Microscopic structures in kaolin subjected to direct shear. Geotechnique, 17(4), pp.309-328.

Nakano, R., 1967. On weathering and change of properties of tertiary mudstone related to landslide. Soils and Foundations, 7(1), pp.1-14.

Neagu, R.C., Cartwright, J. and Davies, R., 2010. Measurement of diagenetic compaction strain from quantitative analysis of fault plane dip. Journal of Structural Geology, 32(5), pp.641-655.

Oertel, G. and Curtis, C.D., 1972. Clay-ironstone concretion preserving fabrics due to progressive compaction. Geological Society of America Bulletin, 83(9), pp.2597-2606.

Paxton, S. T., J. O. Szabo, J. M. Adjukiewicz and R. E. Klimentidis 2002. Construction of an intergranular volume compaction curve for evaluating and predicting compaction and porosity loss in rigid-grain sandstone reservoirs. American Association of Petroleum Geologists Bulletin 86: 2047-2067.

Pickering, K. T., H. Pouderoux, L. C. McNeill, J. Backman, F. Chemale, S. Kutterolf, K. L. Milliken, H. Mukoyoshi, T. J. Henstock, D. E. Stevens, C. Parnell and B. Dugan, 2020. Sedimentology, stratigraphy and architecture of the Nicobar Fan (BengalNicobar Fan System), Indian Ocean: Results from International Ocean Discovery Program Expedition 362. Sedimentology 67(5): 2248-2281.

Philipp, T., Amann-Hildenbrand, A., Laurich, B., Desbois, G., Littke, R. and Urai, J.L., 2017. The effect of microstructural heterogeneity on pore size distribution and permeability in Opalinus Clay (Mont Terri, Switzerland): insights from an integrated study of laboratory fluid flow and pore morphology from BIB-SEM images. Geological Society, London, Special Publications, 454(1), pp.85-106.

Pommer, M. E. and K. L. Milliken 2015. Pore types and pore-size distributions across thermal maturity, Eagle Ford Formation, South Texas. AAPG Bulletin 99: 1713-1744.

Porter, J.R., Knipe, R.J., Fisher, Q.J., Farmer, A.B., Allin, N.S., Jones, L.S., Palfrey, A.J., Garrett, S.W. and Lewis, G., 2000. Deformation processes in the Britannia Field, UKCS. Petroleum Geoscience, 6(3), pp.241-254.

Prawirodirdjo, L., Bock, Y., McCaffrey, R., Genrich, J., Calais, E., Stevens, C., Puntodewo, S.S.O., Subarya, C., Rais, J., Zwick, P. and Fauzi, R.M., 1997. Geodetic observations of interseismic strain segmentation at the Sumatra subduction zone. Geophysical research letters, 24(21), pp.2601-2604.

Proctor, B., Lockner, D.A., Kilgore, B.D., Mitchell, T.M. and Beeler, N.M., 2020. Direct evidence for fluid pressure, dilatancy, and compaction affecting slip in isolated faults. Geophysical Research Letters, 47(16), p.e2019GL086767.

Rabinowitz, H.S., Savage, H.M., Skarbek, R.M., Ikari, M.J., Carpenter, B.M. and Collettini, C., 2018. Frictional behavior of input sediments to the Hikurangi Trench, New Zealand. Geochemistry, Geophysics, Geosystems, 19(9), pp.2973-2990.

Rosenberger, K., Underwood, M.B., Vrolijk, P. and Haines, S., 2020. Data report: clay mineral assemblages in hemipelagic sediments entering the Sumatra subduction zone, IODP Sites U1480 and U1481, Expedition 362. Expedition, 362, p.1.

Rubey, W.W. and King Hubbert, M., 1959. Role of fluid pressure in mechanics of overthrust faulting: II. Overthrust belt in geosynclinal area of western Wyoming in light of fluid-pressure hypothesis. Geological Society of America Bulletin, 70(2), pp.167-206.

Rutter, E.H., Maddock, R.H., Hall, S.H. and White, S.H., 1986. Comparative microstructures of natural and experimentally produced clay-bearing fault gouges. Pure and applied geophysics, 124(1), pp.3-30.

Rybacki, E., Morales, L.F.G., Naumann, M. and Dresen, G., 2014. Strain localization during high temperature creep of marble: The effect of inclusions. Tectonophysics, 634, pp.182-197.

Saffer, D.M. and Bekins, B.A., 2006. An evaluation of factors influencing pore pressure in accretionary complexes: Implications for taper angle and wedge mechanics. Journal of Geophysical Research: Solid Earth, 111(B4).

Saito, S. and Goldberg, D., 2001. Compaction and dewatering processes of the oceanic sediments in the Costa Rica and Barbados subduction zones: estimates from in situ physical property measurements. Earth and Planetary Science Letters, 191(3-4), pp.283-293.

Salman, R., Lindsey, E.O., Feng, L., Bradley, K., Wei, S., Wang, T., Daryono, M.R. and Hill, E.M., 2020. Structural controls on rupture extent of recent Sumatran Fault Zone earthquakes, Indonesia. Journal of Geophysical Research: Solid Earth, 125(2), p.e2019JB018101.

Samsudin, M.S.F., Ariff, Z.M. and Ariffin, A., 2017, April. Deformation behavior of open-cell dry natural rubber foam: Effect of different concentration of blowing agent and compression strain rate. In AIP Conference Proceedings (Vol. 1835, No. 1, p. 020007). AIP Publishing LLC.

Schieber, J. 2016. Experimental testing of the transport-durability of shale lithics and its implications for interpreting the rock record. Sedimentary Geology 331: 162-169. Lithic grains in shale

Schieber, J., J. Southard and K. Thaisen 2007. Accretion of mudstone beds from migrating floccule ripples. Science 3185857: 1760-1763. Floccules in the range of sand-size.

Schmatz, J., Klaver, J., Jiang, M. and Urai, J.L., 2017. Nanoscale morphology of brine/oil/mineral contacts in connected pores of carbonate reservoirs: Insights on wettability from Cryo-BIB-SEM. SPE Journal, 22(05), pp.1374-1384.

Schneider, J., Flemings, P.B., Day-Stirrat, R.J. and Germaine, J.T., 2011. Insights into pore-scale controls on mudstone permeability through resedimentation experiments. Geology, 39(11), pp.1011-1014.

Singh, S.C., Hananto, N., Mukti, M., Robinson, D.P., Das, S., Chauhan, A., Carton, H., Gratacos, B., Midnet, S., Djajadihardja, Y. and Harjono, H., 2011. Aseismic zone and earthquake segmentation associated with a deep subducted seamount in Sumatra. Nature Geoscience, 4(5), pp.308-311.

Sintubin, M., 1994. Clay fabrics in relation to the burial history of shales. Sedimentology, 41(6), pp.1161-1169.

Terzaghi, K., 1925. Principles of soil mechanics: V — physical differences between sand and clay. Engineering News Record 96, 912–915.

Terzaghi, K., Peck, R.B., 1948. Soil Mechanics In Engineering Practice. John Wiley and Sons, New York.

Torres, M. E. and K. Milliken (2019). Linked carbonate cementation and silicate dissolution in the sediments of the Bengal-Nicobar Fan, inputs to the Sumatra subduction zone. prresAmerican Geophysical Union Fall Meeting 2019.

Tunega, D. and Zaoui, A., 2020. Mechanical and bonding behaviors behind the bending mechanism of kaolinite clay layers. The Journal of Physical Chemistry C, 124(13), pp.7432-7440.

Ukar, E. and Cloos, M., 2019. Cataclastic deformation and metasomatism in the subduction zone of mafic blocks-in-mélange, San Simeon, California. Lithos, 346, p.105116.

Van Olphen, H., 1964. Internal mutual flocculation in clay suspensions. Journal of Colloid Science, 19(4), pp.313-322.

Vasseur, G., Djeran-Maigre, I., Grunberger, D., Rousset, G., Tessier, D. and Velde, B., 1995. Evolution of structural and physical parameters of clays during experimental compaction. Marine and petroleum geology, 12(8), pp.941-954.

Velde, B. 1996. Compaction trends of clay-rich deep sea sediments. Marine Geology 133(3-4): 193-201.

Voltolini, M., Wenk, H.R., Mondol, N.H., Bjørlykke, K. and Jahren, J., 2009. Anisotropy of experimentally compressed kaolinite-illite-quartz mixtures. Geophysics, 74(1), pp.D13-D23.

Vrolijk, P., 1990. On the mechanical role of smectite in subduction zones. Geology, 18(8), pp.703-707.

Walker, K.T., Ishii, M. and Shearer, P.M., 2005. Rupture details of the 28 March 2005 Sumatra Mw 8.6 earthquake imaged with teleseismic P waves. Geophysical Research Letters, 32(24).

Wang, X., Jiang, Z., Jiang, S., Chang, J., Zhu, L., Li, X. and Li, J., 2019. Full-scale pore structure and fractal dimension of the Longmaxi shale from the Southern Sichuan Basin: Investigations using FE-SEM, gas adsorption and mercury intrusion porosimetry. Minerals, 9(9), p.543.

Wei, L.I., Jun, X.I.E., GAO, X.H., ZHANG, L.H. and Fang, Y.U., 2008. Characteristics of Jurassic mudstone overpressure and its control on oil and gas accumulation in Turpan Depression. Petroleum Exploration and Development, 35(1), pp.28-33.

Wenk, H.R., Voltolini, M., Kern, H., Popp, T. and Mazurek, M., 2008. Anisotropy in shale from Mont Terri. The Leading Edge, 27(6), pp.742-748.

Worden, R.H., Charpentier, D., Fisher, Q.J. and Aplin, A.C., 2005. Fabric development and the smectite to illite transition in Upper Cretaceous mudstones from the North Sea: an image analysis approach. Geological Society, London, Special Publications, 249(1), pp.103-114.

Yagiz, S., 2001. Overview of classification and engineering properties of shales for design considerations. In Construction and Materials Issues 2001 (pp. 156-165).

Yawar, Z. and J. Schieber 2017. On the origin of silt laminae in laminated shales. Sedimentary Geology 360: 22-34. Shows that coarse silt does segregates from clay in transport but fine silt is part of silt-clay floccules---hence floccules are bigger than fine silt size around 20 microns.

Yong, R.N. and Sheeran, D.E., 1973. Fabric unit interaction and soil behaviour. In Proceedings International Symposium on Soil Structure.

Zakaria, Z., Mohamad Ariff, Z. and Abu Bakar, A., 2018. Monitoring deformation mechanism of foam cells in polyethylene foams via optical microscopy: Effect of density and microstructure. Journal of Cellular Plastics, 54(6), pp.957-976.

Zhou, J., Shrotriya, P. and Soboyejo, W.O., 2004. Mechanisms and mechanics of compressive deformation in open-cell Al foams. Mechanics of Materials, 36(8), pp.781-797.

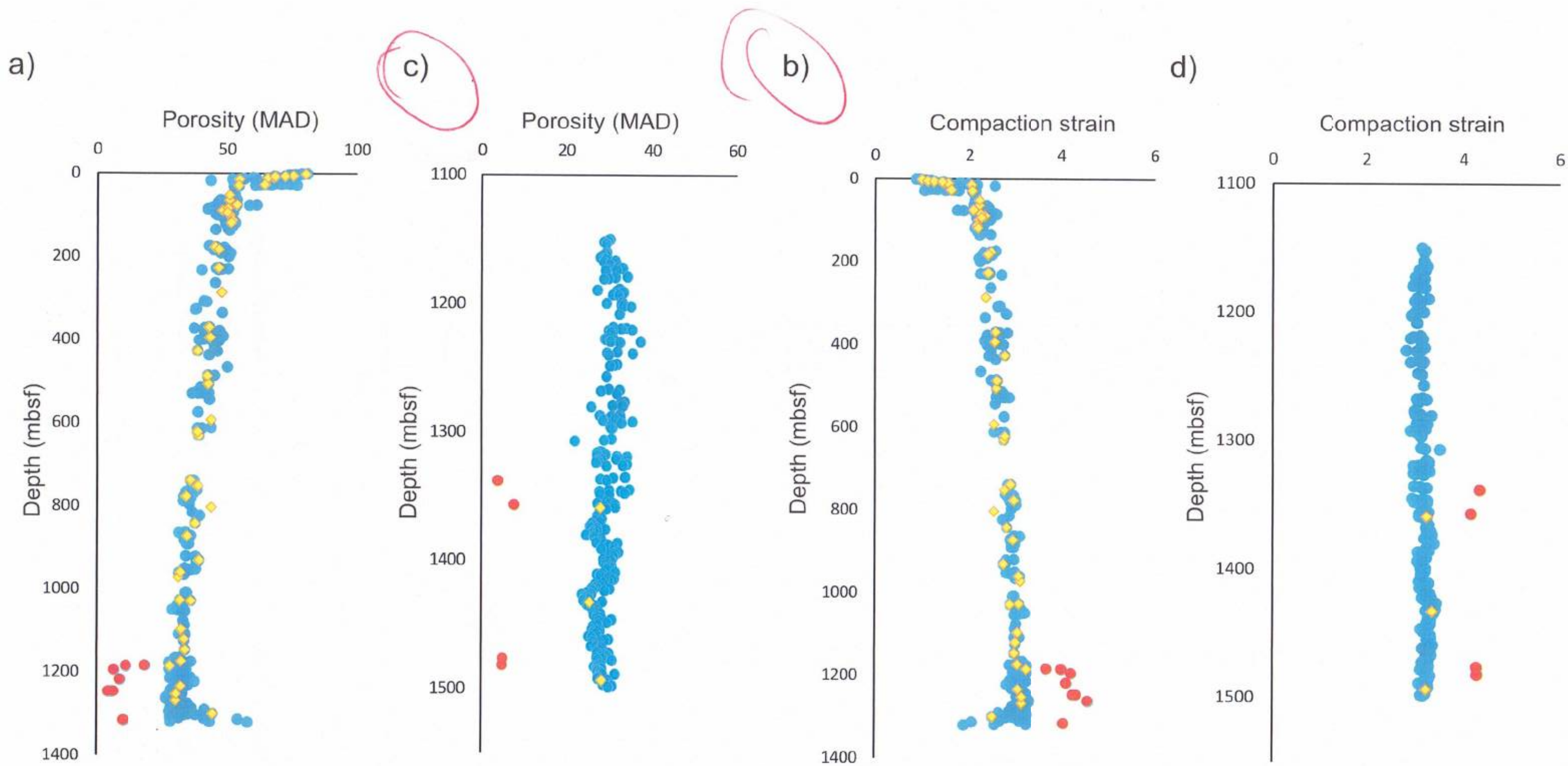

Fig.2: (a) and (b) Shipboard MAD (Moisture and density) porosity vs depth data for mudstone samples recovered from Sites U1480 and U1481; (c) and (d) Cross-plot diagrams for estimated compaction strain vs depth corresponding to samples recovered from Sites U1480 and U1481. Yellow-colored symbols in (a), (b), (c), and (d) show 55 mud samples analyzed at RWTH-Aachen and BEG, Austin. Red-colored points are cemented (concretion) samples.

analyzed by which technique?

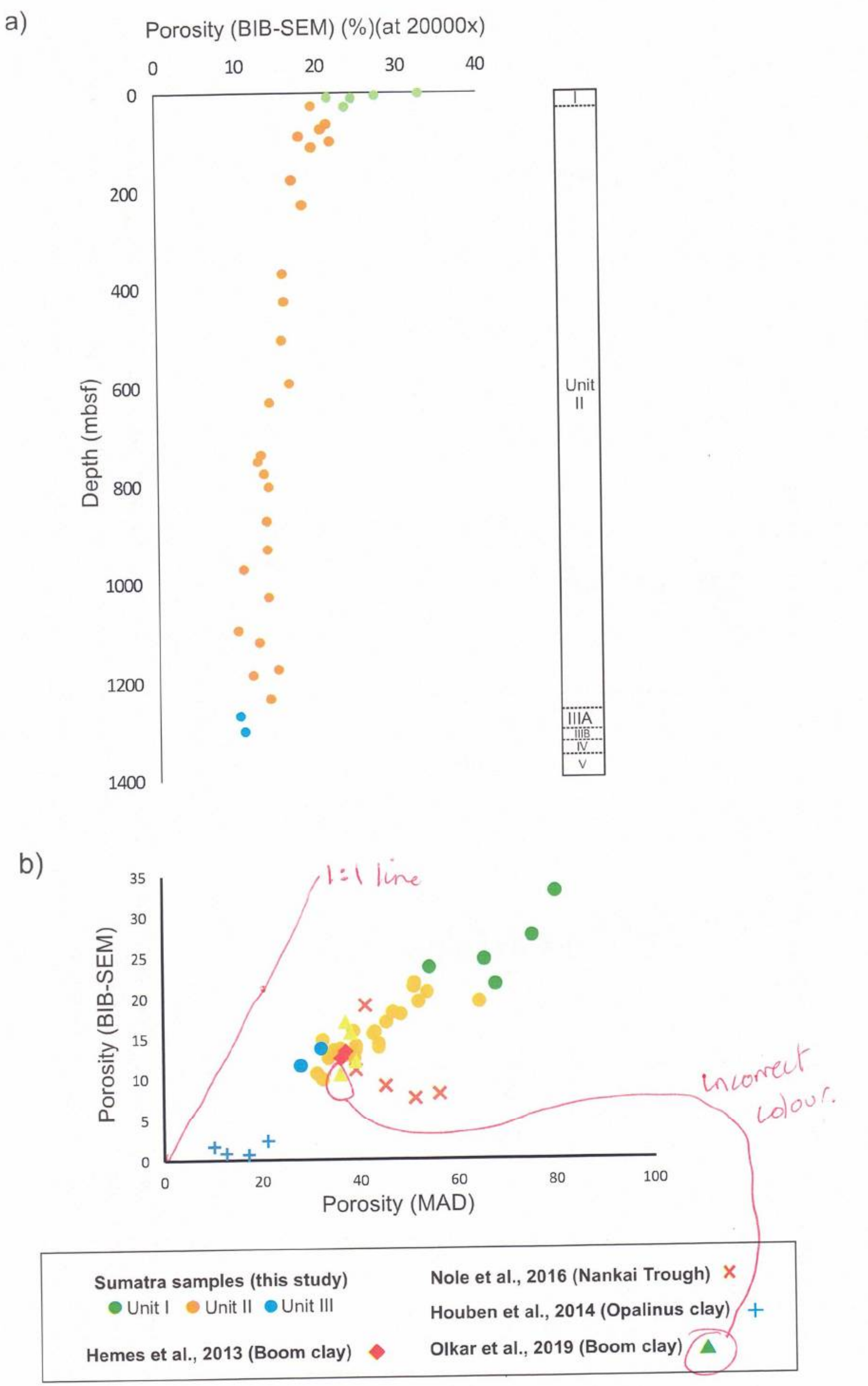

Fig.3: Porosity data for Units I (green dots), II (orange dots), and IIIA (blue dots). (a) BIB-SEM - depth plot. (b) BIB-SEM porosity vs MA porosity. Note: linear relationship that intersects origin. The data estimated by Hemes et al., 2013; Houben et al., 2014; Olkar et al., 2019 also follow similar trend. However, the data estimated by Nole et al., 2016 is deviated from the general trend.

Not convinced tables 2+3 add anything. Supplementary Data? Would prefer to see better mineralogy data either tabulated or graphically or both

Table 2: Summary of pore morphology evolution with depth. Abundant = >25% pores, common = 2%-25% pores, rare = 0-2% pores, absent = not observed.

Depth (mbsf)	Sample no	Clay domain pores								Silt adjacent pores							
				Small pore			Larger pore					Small pore			Larger pore		
		Small pores (<5x10^5 nm^2)	Larger pores (>5x10^5 nm^2)	Elongate linear	Elongate crescent	Equant	Elongate linear	Elongate crescent	Equant	Small pores (<5x10^5 nm^2)	Larger pores (>5x10^5 nm^2)	Elongate linear	Elongate crescent	Equant	Elongate linear	Elongate crescent	Equant
1.24	SN-1	Abundant	Rare	Abundant	Rare	Rare	Rare	Rare	Rare	Abundant	Abundant	Common	Rare	Abundant	Rare	Rare	Abundant
5.10	SN-2	Abundant	Rare	Abundant	Rare	Common	Rare	Rare	Rare	Abundant	Abundant	Common	Rare	Abundant	Common	Common	Abundant
6.25	SN-34	Abundant	Rare	Abundant	Rare	Common	Rare	Rare	Rare	Abundant	Abundant	Rare	Rare	Abundant	Rare	Rare	Abundant
7.21	SN-35	Abundant	Rare	Abundant	Rare	Rare	Rare	Rare	Rare	Abundant	Abundant	Rare	Rare	Abundant	Rare	Common	Abundant
9.18	SN-3	Abundant	Rare	Abundant	Common	Common	Rare	Rare	Common	Common	Abundant	Common	Rare	Abundant	Rare	Common	Abundant
10.69	SN-4	Abundant	Rare	Abundant	Rare	Rare	Rare	Rare	Rare	Common	Abundant	Common	Common	Abundant	Rare	Common	Abundant
14.28	SN-36	Abundant	Rare	Abundant	Rare	Rare	Rare	Rare	Rare	Abundant	Abundant	Common	Common	Abundant	Rare	Common	Abundant
26.05	SN-5	Abundant	Rare	Abundant	Rare	Rare	Rare	Rare	Rare	Abundant	Abundant	Common	Common	Abundant	Rare	Common	Abundant
28.00	SN-6	Abundant	Rare	Abundant	Common	Rare	Rare	Rare	Rare	Abundant	Abundant	Common	Rare	Abundant	Common	Common	Abundant
28.12	SN-37	Abundant	Rare	Abundant	Common	Common	Rare	Rare	Common	Abundant	Abundant	Common	Common	Abundant	Common	Common	Abundant
50.82	SN-38	Abundant	Rare	Abundant	Rare	Common	Rare	Rare	Rare	Abundant	Common	Common	Rare	Abundant	Common	Common	Abundant
63.24	SN-7	Abundant	Rare	Abundant	Common	Rare	Rare	Rare	Rare	Abundant	Abundant	Common	Common	Abundant	Rare	Common	Abundant
74.07	SN-8	Abundant	Rare	Abundant	Common	Rare	Rare	Rare	Rare	Abundant	Abundant	Abundant	Rare	Common	Common	Common	Abundant
83.02	SN-39	Abundant	Rare	Abundant	Common	Common	Common	Rare	Rare	Abundant	Abundant	Common	Common	Abundant	Common	Common	Abundant
87.98	SN-9	Abundant	Rare	Abundant	Common	Rare	Rare	Rare	Rare	Abundant	Abundant	Common	Common	Abundant	Common	Abundant	Abundant
92.82	SN-41	Abundant	Rare	Abundant	Common	Rare	Rare	Rare	Rare	Abundant	Common	Abundant	Common	Common	Common	Common	Common
98.25	SN-10	Abundant	Rare	Abundant	Common	Rare	Rare	Rare	Rare	Abundant	Abundant	Common	Rare	Abundant	Rare	Abundant	Abundant
111.10	SN-11	Abundant	Rare	Abundant	Common	Rare	Rare	Rare	Rare	Abundant	Abundant	Common	Common	Abundant	Common	Common	Abundant
117.13	SN-40	Abundant	Rare	Abundant	Abundant	Rare	Rare	Rare	Rare	Abundant	Common	Abundant	Rare	Common	Common	Common	Common
176.50	SN-12	Abundant	Rare	Abundant	Common	Common	Rare	Rare	Common	Abundant	Abundant	Abundant	Common	Common	Common	Common	Common
182.62	SN-42	Abundant	Rare	Abundant	Common	Rare	Rare	Rare	Rare	Abundant	Abundant	Common	Common	Abundant	Common	Common	Abundant
226.70	SN-13	Abundant	Rare	Abundant	Abundant	Rare	Rare	Rare	Rare	Abundant	Common	Common	Common	Common	Common	Common	Abundant
285.51	SN-43	Abundant	Rare	Abundant	Common	Rare	Rare	Rare	Rare	Abundant	Common	Abundant	Rare	Common	Common	Common	Abundant
369.19	SN-14	Abundant	Rare	Abundant	Common	Rare	Rare	Rare	Rare	Common	Common	Abundant	Rare	Common	Common	Common	Common
394.01	SN-44	Abundant	Rare	Abundant	Abundant	Rare	Rare	Rare	Rare	Abundant	Abundant	Common	Common	Abundant	Common	Common	Abundant
426.68	SN-15	Abundant	Rare	Abundant	Common	Rare	Rare	Rare	Rare	Common	Common	Abundant	Common	Common	Abundant	Common	Common
486.72	SN-45	Abundant	Rare	Abundant	Common	Common	Rare	Rare	Rare	Abundant	Common	Abundant	Rare	Common	Abundant	Common	Common
505.32	SN-16	Abundant	Rare	Abundant	Common	Rare	Rare	Rare	Common	Common	Common	Abundant	Common	Common	Common	Rare	Common
592.42	SN-17	Abundant	Rare	Abundant	Abundant	Rare	Rare	Rare	Rare	Abundant	Common	Common	Rare	Common	Common	Common	Common
621.2	SN-46	Abundant	Rare	Abundant	Abundant	Rare	Rare	Rare	Rare	Common	Common	Abundant	Common	Rare	Abundant	Common	Common
630.55	SN-18	Abundant	Rare	Abundant	Common	Rare	Rare	Rare	Rare	Common	Common	Abundant	Common	Common	Abundant	Rare	Common
737.39	SN-19	Abundant	Rare	Abundant	Abundant	Rare	Rare	Rare	Rare	Common	Common	Common	Common	Rare	Common	Common	Common
737.47	SN-47	Abundant	Rare	Abundant	Abundant	Rare	Rare	Rare	Rare	Common	Common	Abundant	Rare	Common	Abundant	Common	Common
751.16	SN-20	Abundant	Rare	Abundant	Abundant	Rare	Rare	Rare	Rare	Common	Common	Abundant	Common	Rare	Abundant	Common	Rare
776.17	SN-21	Abundant	Rare	Abundant	Common	Rare	Rare	Rare	Rare	Common	Common	Common	Common	Common	Abundant	Common	Rare
802.55	SN-22	Abundant	Rare	Abundant	Abundant	Rare	Rare	Rare	Rare	Common	Common	Abundant	Common	Common	Common	Abundant	Common
841.56	SN-48	Abundant	Rare	Abundant	Abundant	Rare	Rare	Rare	Rare	Common	Common	Abundant	Rare	Common	Abundant	Rare	Rare
871.87	SN-23	Abundant	Rare	Abundant	Abundant	Rare	Rare	Rare	Rare	Common	Common	Abundant	Common	Rare	Common	Common	Common